Design and Characterization of Biomimetic Artificial Hair Cells in an Artificial Cochlear Environment

Jeffrey Philip Travis

Thesis submitted to the faculty of the Virginia Polytechnic Institute and State University in partial fulfillment of the requirements for the degree of

Master of Science
in
Mechanical Engineering

Donald J. Leo, Chair

John W. Grant

Pablo A. Tarazaga

February 17, 2014
Blacksburg, Virginia

Keywords: artificial hair cell, dynamic response, lipid bilayer, cochlear environment

Design and Characterization of Biomimetic Artificial Hair Cells in an Artificial Cochlear Environment

Jeffrey Philip Travis

Abstract

This research details the creation and characterization of a new biomimetic artificial inner hair cell sensor in an artificial cochlear environment. Designed to mimic the fluid flows around the inner hair cells of the human cochlea, the artificial cochlear environment produces controlled, linear sinusoidal fluid flows with frequencies between 25 and 400 Hz. The lipid bilayer-based artificial inner hair cell generates current through changes in the bilayer's capacitance. This capacitance change occurs as the sensor's artificial stereocilium transfers the force in the fluid flow to the bilayer.

Frequency tuning tests are performed to characterize the artificial inner hair cell's response to a linear chirp signal from 1 to 400 Hz. The artificial inner hair cell's response peaks at a resonant frequency of approximately 83 Hz throughout most of the tests. Modelling the artificial stereocilium as a pinned free beam with a rotational spring at the pinned end yields a rotational spring stiffness of $177 * 10^{-6}\ Nm/rad$. Results with 0 mV potential applied across the bilayer indicate that current generation at 0 mV likely comes from other sources besides the bilayer. Increasing the voltage potential increases the broadband power output of the system, with an approximately linear relationship. A final test keeps the fluid flow frequency constant and varies the fluid velocity and applied voltage potential. Manipulation of the applied voltage potential results in a fluid velocity to RMS current relationship reminiscent of the variable sensitivity of the human cochlea.

Acknowledgements

Several people have been instrumental to my success at Virginia Tech. First and foremost, I would like to thank Dr. Leo, my advisor, for the opportunity to work with him on such an exciting project. His guidance through the entire research process allowed me to excel as a graduate student. I would like to thank Dr. Grant and Dr. Tarazaga for their significant contributions to my research. I would also like to thank my colleagues in the Biomolecular Materials and Systems Laboratory (BMSL). Each member of the BMSL team helped me along the way, and I would have not finished my research without them.

The role my family and friends have played in the completion of my thesis cannot be understated. I would not be the person I am today without their heartfelt support. Finally, I would like to thank Emily Mikkelson for her continual motivation and encouragement.

Table of Contents

List of Figures

List of Tables

List of Abbreviations

ACE	Artificial Cochlear Environment
AIHC	Artificial Inner Hair Cell
CPSD	Cross Power Spectral Density
DAQ	Data Acquisition
DC	Direct Current
DPhPC	Diphytanoyl Phosphocholine
FEA	Finite Element Analysis
IHC	Inner Hair Cell
KCl	Potassium Chloride
MOPS	4-Morpholinepropanesulfonic Acid
PEG-DMA	Polyethylene Glycol Dimethacrylate
RAM	Regulated Attachment Method
UV	Ultraviolet

1 Introduction and Background

1.1 Cochlear Mechanics

The human ear consists of three main parts that are termed the outer, middle, and inner ear. Sound enters the outer ear and travels through the auditory canal until it contacts the tympanic membrane, which physically separates the outer and middle ear. The ossicles are tiny bones in the middle ear and act to transmit the vibrations in the air to the fluid in the inner ear, or the cochlea. Perilymph and endolymph are the two fluids that fill the cochlea. Both fluids have physical properties very similar to water [1].

The majority of research in hearing mechanics focusses on the cochlea because of its critical role in hearing. The cochlea is a snail-shaped coil of three tubes called the scala vestibuli, scala media, and scala tympani. A common simplified model of the cochlea is two straight tubes, where the scala vestibuli and scala media are combined into one [1]. This simplification can occur because the thin, flexible membrane separating the scala vestibuli and scala media has a negligible impact on the fluid motion in the cochlea. These two sections of the simplified cochlear model are separated by the basilar membrane. When a vibration enters the fluid-filled cochlea, a pressure difference occurs between the scala tympani and the combined scala vestibuli and scala media. This pressure difference causes a wave to travel from the basal to distal end of the basilar membrane. The varying width and stiffness along the length of the basilar membrane cause the traveling wave to peak at a particular location based on the vibration's frequency. This peak occurs where the vibration frequency in the fluid matches the resonant frequency of that particular location along the basilar membrane.

Along the entire surface of the basilar membrane sits the organ of Corti. A few of the important parts of the organ of Corti are the reticular lamina, the tectorial membrane, and the hair cells. Because of their geometry and connection to one another, as the basilar membrane moves up and down, the tectorial membrane moves laterally back and forth. The top of the hair cells, which are connected to the reticular lamina, move with the same lateral motion. Tiny hairs called stereocilia protrude from the top of the hair cells. The stereocilia of the outer hair cells contact the tectorial membrane while the inner hair cell (IHC) stereocilia only extend into the gap between the reticular lamina and the tectorial membrane. The shear of these stereocilia causes the mechanosensitive hair cells to be excited and generate a signal in the auditory nerve fibers. The brain interprets this signal as a sound with amplitude and frequency dependent on the amount of stereocilia shear and the hair cell location along the basilar membrane. IHCs are responsible for approximately 90 percent of the auditory signals sent to the brain [1]. Shear is induced in the IHC stereocilia by a combination of viscous drag between the stereocilia as they move in the fluid and the fluid flow in the gap between the reticular lamina and the tectorial membrane [2].

One of the many interesting characteristics of the cochlea is its variable sensitivity to sound pressure level, a measure of sound intensity. As sound intensity increases past a certain sound pressure level, the signal magnitude sent from the auditory nerve fibers starts to level off. Past a certain point, in fact, the auditory signal starts to decrease [3]. Dallos directly probed the outer and inner hair cells of a guinea pig to obtain the auditory receptor potential as he increased the sound pressure level. Figure 1-1 shows the results of one of Dallos's tests for an IHC at the location along the cochlea that responded best to the 800 Hz burst sound signal acting as the input stimulus. The variable sensitivity of the mammalian cochlea is seen in the relatively linear

increase, plateau, and eventual decrease of the receptor potential as sound pressure level increases. The variable sensitivity of the cochlea allows a larger range of sound intensities to be interpreted by the cochlea than if cochlear sensitivity were completely linear.

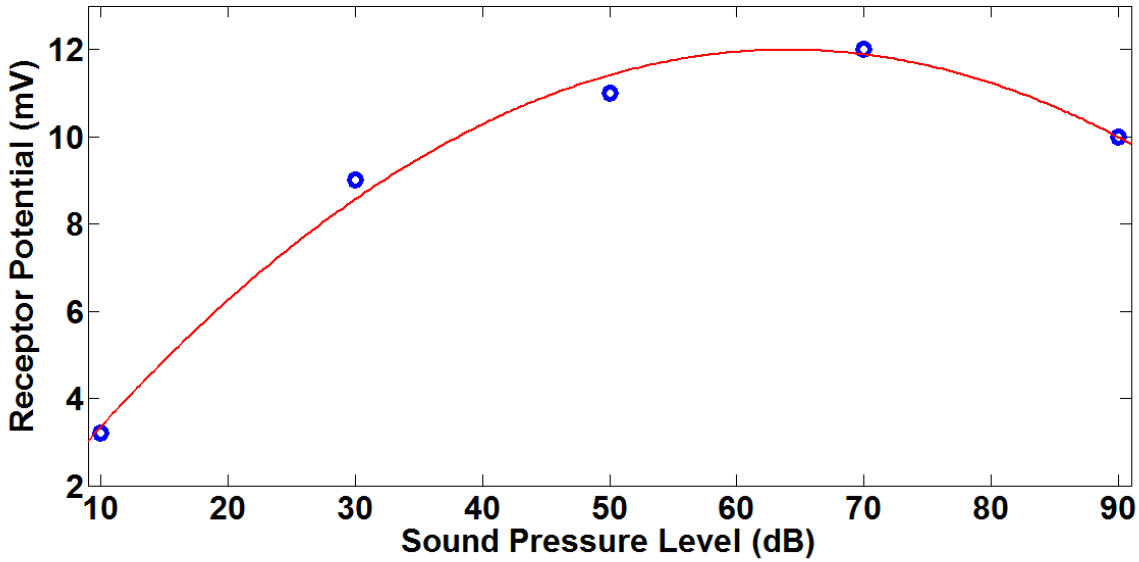

Figure 1-1. AC receptor potential as a function of sound pressure level for an IHC in the cochlea of a guinea pig. The nonlinear gain of the cochlea is seen in the plateau and eventual decrease in the receptor potential as sound pressure level increases. The receptor data was recorded as a response to a burst sound signal at 800 Hz. The location of the receptors along the cochlea had a resonant frequency of 800 Hz. The blue markers indicate the collected data while the red line is the 2nd order polynomial trend line fit to the data. The plot is recreated from data presented by Dallos [3].

1.2 Physical Cochlear Models

Many physical models of the cochlea have been developed in the past several decades to better understand different cochlear functions. One of the first physical models of the cochlea was developed in 1975 by Chadwick [4]. His cochlear model featured two straight fluid-filled chambers separated by a thin elastic beam representing the basilar membrane. Chadwick's group confirmed the idea of basilar membrane tonotopicity, the spatial mapping of sound frequencies. The first group to create a scale model of the human cochlea was from the Polytechnic

University of Turin in 1985 [5]. The 50:1 model from Turin featured three chambers and a full organ of Corti. Their results showed that basilar membrane tonotopicity was determined primarily by basilar membrane stiffness and not the physical properties of the organ of Corti.

In 1993, Lechner created a model of the basilar membrane with only one fluid channel [6]. Lechner found that the inclusion of nonlinear feedback transducers added a sharpening effect to the frequency response and that the use of only one fluid channel did not greatly affect the basilar membrane response. Also in 1993, Zhou created the first life-sized physical model of the human cochlea [7]. Zhou's results on basilar membrane response curves showed similarity to previous research on the cochlea in a human cadaver. More work on life-sized cochlea has also been completed in recent years [8-11]. Much of this recent work has used improved models of the basilar membrane to obtain more realistic results. Two recent physical models of the cochlea, developed by Chen in 2006 [12] and Liu in 2008 [13], demonstrated many of the same characteristics of the human cochlea while not using a life-sized model.

Although several recent physical models of the cochlea have been developed, the focus of these models has been the response of the basilar membrane. A physical model of hair cell stereocilia excitation, the mechanism directly responsible for auditory nerve excitation, has yet to be created. Just like the previously completed research on the basilar membrane, creating a physical model of the stereocilia would further the understanding of a vital cochlear function. A physical model of stereocilia excitation could also be used to validate and support the current simulation research on stereocilia and their corresponding hair cells. As IHCs generate the majority of auditory nerve signals and IHC stereocilia excitation mechanisms are the least understood of the cochlear hair cell stereocilia, an IHC stereocilia physical model would provide great benefit to

the scientific community. A realistic physical model of the environment surrounding the IHCs in the cochlea is also needed.

1.3 Lipid Bilayers

Lipid bilayers are the basis of the sensing technology used in the artificial inner hair cells (AIHCs) created in this work. Lipid bilayers form the membranes between almost all cells in nature and have unique properties that make them useful in the application of bio-inspired sensing. A lipid bilayer is composed of two self-assembling lipid monolayers. A lipid monolayer naturally forms when an aqueous droplet containing phospholipids is surrounded by an immiscible fluid, such as oil. Phospholipids, with their hydrophilic head group and hydrophobic tail group, orient themselves with their tails facing outward from the aqueous droplet. This configuration of the phospholipids is shown in Figure 1-2a. Figure 1-2 displays the configurations of lipid monolayers and bilayers.

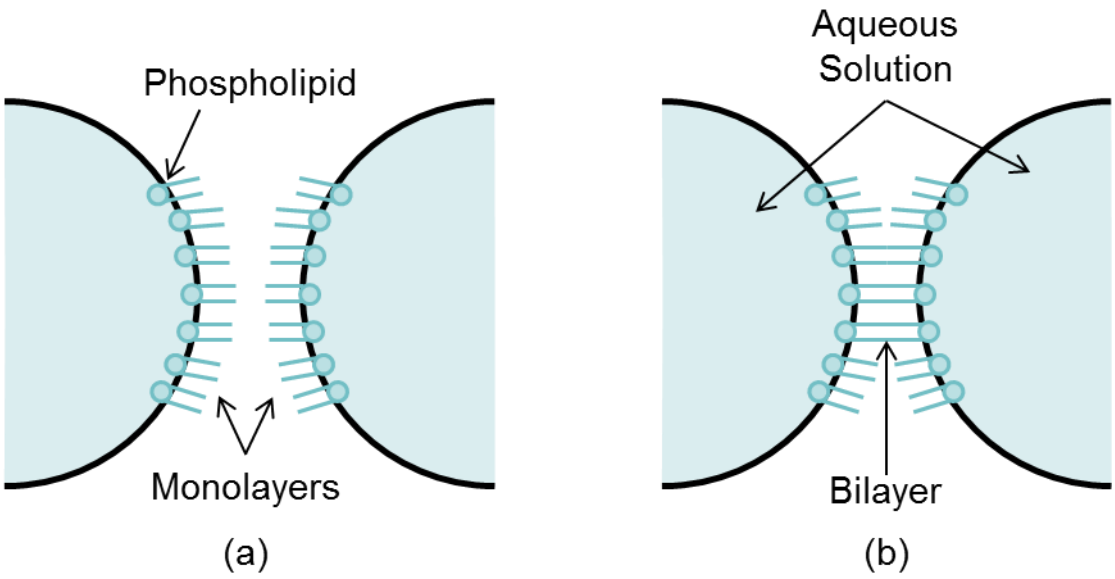

Figure 1-2. Diagram of monolayer and bilayer formations. (a) shows the monolayer that naturally forms after a short amount of time when a phospholipid-containing aqueous droplet is surrounded by an immiscible fluid. Also displayed in (a) are several phospholipids which make up the monolayers. The phospholipid is oriented with the head group facing in towards the aqueous solution. (b) shows the bilayer that forms a short time after the two monolayers are brought into contact.

Once two monolayers form and are brought into contact, a bilayer assembles as the immiscible fluid is expelled between the monolayers and the phospholipid tail groups "zip" together. The resulting lipid bilayer has electrical properties that resemble that of a parallel-plate capacitor. The electrical equivalent and corresponding theory of the lipid bilayer system is discussed in Section 2.1. Small perturbations in the aqueous droplets can cause relatively large changes in the bilayer area and capacitance. Thus, lipid bilayers can act as variable capacitors in a variety of sensing applications.

Lipid bilayers have been used in the creation of a number of bio-inspired materials developed by Dr. Leo's group at Virginia Tech [14-20]. Specifically, the Virginia Tech group has previously developed a hair cell sensor to detect air flow [19] as well as fluid flow [16]. For the hair cell sensor created by Sarles et al. to detect air flow, a lipid bilayer was formed between a hydrogel

and an aqueous droplet [19]. The hydrogel acted as the base of a synthetic hair which vibrated due to a constant air flow past the hair. Sarles found that the force from the vibrating hair was large enough to shake the hydrogel and change the bilayer area, thus generating a current in the sensor. Pinto found similar results when testing a different version of the hair cell sensor subjected to a constant fluid flow in water [16]. The construction of the hair cell sensor in this work takes its inspiration from Sarles's work. A detailed description of the hair cell sensor is given in Section 3.1. These new hair cell sensors are tested in a fluid environment that more closely resembles that of the human cochlea, with a fully-submerged sensor and sinusoidal fluid flows.

1.4 Research Objectives

This work presents the results of testing a lipid bilayer-based artificial inner hair cell (AIHC) in an artificial cochlear environment (ACE). The primary goal of this research is to develop an AIHC that senses the sinusoidal fluid flows produced in the ACE. To accomplish this goal, the work begins by investigating if the ACE can mimic the fluid environment around the IHC stereocilia. Mimicking the cochlear environment requires the ACE to create sinusoidal fluid flows at a variety of flow velocities and frequencies. The main objective for the AIHC is the development of a lipid bilayer-based hair cell sensor that can output a current in response to a sinusoidal fluid excitation. Testing of the sensing capabilities of the AIHC includes control tests that seek to determine which aspects of the AIHC are important to its current generation capabilities.

The third research objective is to characterize the AIHC. To fully assess its capabilities, the AIHC's response to different fluid velocities, fluid frequencies, and applied potential across its bilayer is tested. The final research objective addressed in this work involves recreating the

variable sensitivity of the human cochlea in the AIHC, which requires the AIHC's output to reproduce the general nonlinear shape of the receptor potential output in Figure 1-1.

This work begins with a review of some of the relevant theoretical topics, found in Chapter 2. Chapter 3 gives a thorough description of the experimental methods used in this work. AIHC and ACE creation are outlined, as well as the experimental setup, testing procedures, and data analysis techniques. The results of testing the AIHC in the ACE are presented in Chapter 4. A quantitative description of the fluid flows in the ACE is discussed, followed by a presentation of the response of the AIHC under a variety of conditions.

2 Theoretical Discussion

2.1 Lipid Bilayer Current Generation

A lipid bilayer has often been represented as an electrical circuit with a resistor in parallel with a capacitor [19, 21, 22]. A diagram showing the bilayer and aqueous droplets is displayed in Figure 2-1. Figure 2-1a shows a lipid bilayer formed between two aqueous droplets. Oil immiscible with water surrounds both aqueous droplets. Figure 2-1b gives the equivalent electrical circuit of the system consisting of the two aqueous droplets and the bilayer. Because the resistance of the aqueous solution, R_s, is relatively low and the bilayer resistance, R_b, is high, the current through the cell membrane system can be determined solely by the bilayer capacitance, C_b.

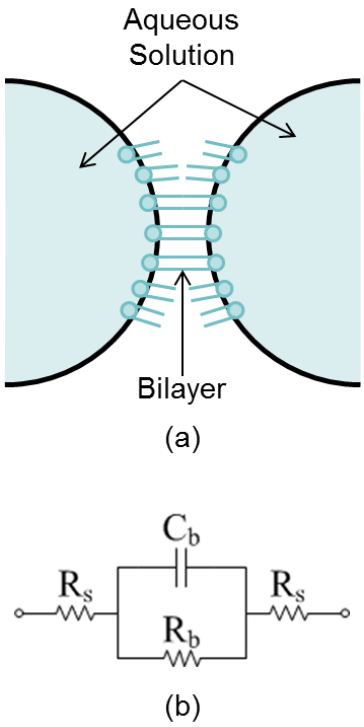

Figure 2-1. Diagram of a lipid bilayer formed between two droplets full of aqueous solution, (a), and the equivalent electrical circuit, (b). Immiscible oil surrounds the two aqueous droplets. (b) shows the resistances and capacitances of the lipid bilayer, with the subscript b designating the bilayer and the subscript s designating the aqueous solution.

The charge contained in a purely capacitive system is given by

$$Q = CV \tag{2-1}$$

where C is the capacitance of the system and V is the voltage applied across the system. Therefore, the current through a lipid bilayer is the time rate of change of the charge defined in Equation (2-1). Since a constant voltage is applied across the lipid bilayers used in this work, the current through the bilayer is given by

$$i(t) = \frac{dC(t)}{dt}V \tag{2-2}$$

The bilayers in this work are physically deformed by a force exerted on them. As the force is applied, the area of the bilayer changes, directly altering the bilayer's capacitance. When a constant potential is applied across a lipid membrane containing solvents, the electrowetting effect also plays a role in changes in bilayer area [23, 24]. As the applied potential increases or decreases, the bilayer area changes. Considering the electrowetting effect, the capacitance across the bilayer is given by

$$C(V,t) = C_0(t)(1 + \alpha V^2) \tag{2-3}$$

where C_0 is the capacitance of the bilayer with 0 mV potential applied across the bilayer and α is the voltage dependence of the bilayer. The potential applied across the bilayer is also referred to as the direct current (DC) offset. When substituting Equation (2-7) into Equation (2-2), the current through the lipid bilayer is given by

$$i(V,t) = \left(\frac{dC_0(t)}{dt}\right)V + \left(\alpha\frac{dC_0(t)}{dt}\right)V^3 \tag{2-4}$$

Therefore, the current through the bilayer is both a linear and cubic function of the DC offset. The results discussed in Chapter 0 investigate the bilayer voltage dependence of the AIHC and whether the relationship between the DC offset and produced current is more linear or cubic.

2.2 Fluid Flow in the Artificial Cochlear Environment

2.2.1 Fluid Flow Characterization

A number of nondimensional parameters are used to characterize the fluid flow in the ACE and around the artificial stereocilium. The Reynolds number and Womersley number are the first two parameters chosen to describe the fluid flow. Both of these parameters, along with geometric and boundary condition similarity, are used to describe the level of dynamic similarity in a fluid flow system. The Reynolds number quantifies the relative relationship between inertial and viscous forces and is given by

$$Re = \frac{UL}{\nu} \tag{2-5}$$

where U is the fluid velocity, L is the characteristic length, and ν is the kinematic viscosity of the fluid [25]. The second parameter of interest in quantifying the fluid flow is the Womersley number, given by

$$\alpha = L\sqrt{\frac{2\pi f}{\nu}} \tag{2-6}$$

where f is the frequency of the oscillatory flow [26]. In the case of fluid flow around the stereocilium, the characteristic length is the stereocilium diameter. When describing fluid flow through a duct, the characteristic length is the duct diameter. The Womersley number is useful in determining the relative importance of transient inertial forces to shear forces in an oscillatory flow. The use of nondimensional parameters to describe the sinusoidal fluid flow allows direct

comparison between the biological case in the human cochlea and the artificial case in the test setup.

Two additional fluid flow parameters are used to quantify the linearity of the flow field. The Keulegan-Carpenter number and the frequency parameter are used to determine if the flow field is symmetric or asymmetric. In an asymmetric flow field, vortex shedding occurs and nonlinearities are observed. The Keulegan-Carpenter number is given by

$$KC = \frac{U}{Lf} \tag{2-7}$$

The frequency parameter is the ratio of the Reynolds number to the Keulegan-Carpenter number and is given by

$$\beta = \frac{Re}{KC} \tag{2-8}$$

In general, low values of the frequency parameter ($\beta<10$) along with low values of the Keulegan-Carpenter number ($KC<10$) describe a symmetric flow field. For a sinusoidal fluid flow, a symmetric flow field is characterized by a purely sinusoidal force exerted on the stereocilium. When nonlinearities and vortex shedding arise in the flow field, variations in the force curve can occur. These variations, in the form of higher-order harmonics, non-periodicities, and out-of-plane forces, cannot be determined through empirical means and must be calculated using computational fluid dynamics [27]. Since these simulations would need to be executed for each *β-KC* pair, the time required to calculate the fluid force on the stereocilium would greatly increase. Therefore, it is desirable in this work to remain in a *β-KC* range indicative of a symmetric flow field.

2.2.2 Fluid Flow around the Artificial Stereocilium

One of the main challenges in characterizing the AIHC is determining the fluid velocity in the ACE, and, more specifically, the fluid flow around the AIHC's artificial stereocilium. There are four steps in determining the fluid flow around the artificial stereocilium:

- Calculating the volume velocity at the input of the duct
- Defining the velocity profile
- Finding the entrance length
- Predicting if asymmetries in the flow field will occur

Before calculating the fluid velocity around the artificial stereocilium in the middle of the duct, the volume velocity at the entrance or beginning of the duct must be determined. In the experimental setup introduced in Section 3.2, a rigid plug is attached to a flexible membrane at the duct inlet. The volume velocity at the entrance of the duct is dependent on the velocity of the input plug, the size of the input plug, and the flexibility of the membrane covering the duct inlet and is given by

$$Q_{in} = U_{plug} A_{eff} \tag{2-9}$$

where U_{plug} is the velocity of the input plug and A_{eff} is the effective input area. For the case of a highly-flexible membrane, as is discussed in Section 3.2, and small input displacements, discussed in Chapter 0, the areas of the flexible membrane away from the plug are unaffected by the plug vibration. Therefore, the input membrane provides no additional surface area to A_{eff} in Equation (2-9), and the effective input area is the plug area.

The steady state fluid flow velocity profile in a square duct driven by a sinusoidal pressure gradient is described by

$$\tilde{w}(\xi,\zeta,t) = \frac{w}{K/\omega} \tag{2-10}$$
$$= \frac{16}{\pi^2}\sum_{m=0}^{\infty}\sum_{n=0}^{\infty}\frac{(-1)^{m+n}}{(2m+1)(2n+1)}\cos\left(\frac{(2m+1)\pi}{2}\xi\right)\cos\left(\frac{(2n+1)\pi}{2}\zeta\right)[m,n]$$

where *w* is the fluid velocity in the duct and the pressure gradient forcing function is given by

$$f(t) = -K\cos(\omega t) \tag{2-11}$$

where *K* is the maximum pressure gradient at the duct inlet and ω is the oscillation frequency [28]. [*m*,*n*] from Equation (2-10) is given by

$$[m,n] = \frac{\psi\left(\frac{\pi^2}{4}\right)[(2m+1)^2+(2n+1)^2]\cos(\omega t)+\psi^2\sin(\omega t)}{\psi^2+\frac{\pi^4}{16}[(2m+1)^2+(2n+1)^2]^2} \tag{2-12}$$

where ψ is a dimensionless frequency parameter given by

$$\psi = \frac{a^2\omega}{\nu} \tag{2-13}$$

where *a* is half the duct width and *v* is the fluid's kinematic viscosity. ξ and ζ from Equation (2-10) describe the position in the duct at which the fluid velocity is evaluated and are given by

$$\xi = \frac{x}{a} \tag{2-14}$$

where *x* is the horizontal position in the duct from center and

$$\zeta = \frac{y}{a} \tag{2-15}$$

where *y* is the vertical position in the duct from center. Inspection of Equations (2-10) through (2-15) reveals that the velocity profile is independent of the maximum pressure gradient.

Entrance length is defined as the distance from the entrance of a pipe after which the velocity profile is fully developed [25]. In the case of an oscillatory flow, an underdeveloped velocity

profile exhibits higher order harmonics of the driving frequency [29]. Only after the entrance length distance from the input will the oscillatory flow consist solely of the driving frequency. The entrance length for a circular duct experiencing oscillating flow can be estimated by

$$L_e = 0.00219ReD \tag{2-16}$$

where *D* is the duct diameter [29, 30]. The hydraulic diameter, which is equal to the side length of a square duct, can be used as an estimate for the diameter in Equation (2-16) [25]. If the entrance length is longer than the distance from the duct input to the artificial stereocilium, then the assumption that the fluid velocity is given by Equation (2-10) is invalid. The second assumption that must be met to maintain that Equation (2-10) describes the fluid field is the lack of asymmetries. The development of asymmetries is determined by the frequency parameter β and the Keulegan-Carpenter number *KC*, which are discussed in Section 2.2.1.

If the assumptions of a linear flow field and an entrance length shorter than the distance from the duct inlet to the artificial stereocilium are met, then the velocity around the artificial stereocilium can be solved by applying the volume velocity to the velocity profile described by Equation (2-10). For example, if velocity profile showed an even velocity distribution, the fluid velocity around the stereocilium would be equal at all points along the stereocilium and given by

$$U_s = \frac{Q_{in}}{A_{duct}} \tag{2-17}$$

where A_{duct} is the area of the duct cross section. For uneven velocity distributions, the fluid velocity would need to be calculated for multiple positions along the stereocilium.

2.3 Artificial Stereocilium Resonant Frequency

Calculation of the resonant frequencies of the tapered artificial stereocilium in the AIHC lacks a closed form solution and thus requires the use of more advanced methods. The Rayleigh-Ritz method allows the resonant frequencies of a tapered beam to be computed using five steps:

- Defining the system's boundary conditions
- Choosing appropriate admissible functions
- Determining the system's potential and kinetic energies
- Forming the mass and stiffness matrices
- Solving the eigenvalue problem to calculate the system's natural frequencies

Two different boundary conditions for the attachment of the artificial stereocilium in the AIHC are explored when solving the natural frequencies. The first boundary condition is an ideal clamped beam. The second boundary condition is a pinned beam with a torsional spring attached at the pinned end. Figure 2-2 shows an image of the two boundary condition assumptions. The stiffness of the rotational spring is represented by τ in Figure 2-2b. The geometric boundary conditions for the clamped beam in Figure 2-2a are given by

$$w(0,t) = w_x(0,t) = 0 \tag{2-18}$$

where $w(0,t)$ is the lateral displacement of the beam at location $x = 0$ at time t and $w_x(0,t)$ is the derivative with respect to x of the displacement, or slope, of the beam at location $x = 0$ and time t. The lateral displacement of the beam is also shown in Figure 2-2b. The only geometric boundary condition for the beam in Figure 2-2b is given by

$$w(0,t) = 0 \tag{2-19}$$

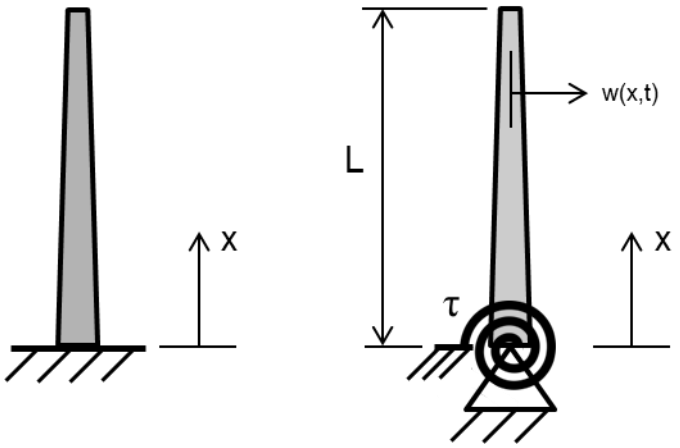

Figure 2-2. Diagram showing the tapered beam represented as a clamped-free beam in (a) and a pinned-free beam with a rotational spring attached at the pinned end in (b). The rotational stiffness of the spring is given by τ. $w(x,t)$ gives the lateral displacement of the beam at location x and time t. The location $x = 0$ corresponds to the clamped or pinned end while $x = L$ represents the free end of the beam.

Natural boundary conditions, such as the amount of force or moment present at certain locations along the beam, can also be defined. However, only the geometric boundary conditions need to be satisfied in the choice of admissible functions. The series of admissible functions chosen for the clamped-free tapered beam is given by

$$z_i(x) = x^{i+1} \text{ for } i = 1, 2, 3 \ldots 8 \tag{2-20}$$

Using an admissible function with a high number of terms increases the accuracy and allows for a greater number of natural frequencies to be calculated. The admissible functions chosen for the pinned-free beam with a rotational spring attached to the pinned end is given by

$$z_i(x) = \left(\frac{x}{L}\right)^i \text{ for } i = 1, 2, 3 \ldots 8 \tag{2-21}$$

where L is the length of the beam, as shown in Figure 2-2. Both Equation (2-20) and (2-21) maintain the geometric constraints listed in Equations (2-18) and (2-19), respectively. Using the Rayleigh-Ritz method, these series of admissible functions are used to estimate the shape of the

beam in motion. Thus, the admissible functions are used in place of the displacement term in Figure 2-2.

Once the admissible functions are used to replace the beam displacement, the maximum kinetic energy for both the clamped-free beam and pinned-free beam is given by

$$T_{max} = \frac{1}{2}\int_0^L \rho A(x) z^2 dx \tag{2-22}$$

where $A(x)$ is the cross section area at location x and *z* is the series of admissible functions from Equation (2-20) or (2-21), depending on the boundary conditions. The maximum potential energy in the case of the clamped-free beam is given by

$$V_{max} = \frac{1}{2}\int_0^L EI[z'']^2 dx \tag{2-23}$$

where *E* is the elastic modulus of the beam, *I* is the beam's moment of inertia, and z'' is the second derivative of the admissible function with respect to *x*. The addition of the rotational spring in the pinned-free beam case requires that the potential energy of the spring be included in the equation for maximum potential energy. The maximum potential energy for the pinned-free beam with a rotational spring at the pinned end is given by

$$V_{max} = \frac{1}{2}\int_0^L EI[z'']^2 dx + \frac{1}{2}\tau[z'(0)]^2 \tag{2-24}$$

where $z'(0)$ is the first derivative with respect to x, or slope, of the admissible function at location $x = 0$. The slope can be used in place of the angular rotation of the spring in Equation (2-24) if a small rotational displacement is assumed. In such a case, the small angle approximation states that

$$z'(0) = \tan\theta \approx \theta \tag{2-25}$$

With the kinetic and potential energies of both boundary condition cases defined, the mass and stiffness matrices can be formed. The mass matrix is the same for each boundary layer condition and is given by

$$M_{ij} = \frac{1}{2}\int_0^L \rho A(x) z^2 dx = \frac{1}{2}\int_0^L \rho A(x) z^T z dx \tag{2-26}$$

where z^T is the transpose of the series of admissible functions. The stiffness matrices are formed from the maximum potential energy equations from Equations (2-23) and (2-24). For the clamped-free beam, the stiffness matrix is given by

$$K_{ij} = \frac{1}{2}\int_0^L EI[z'']^2 dx = \frac{1}{2}\int_0^L EI z''^T z'' dx \tag{2-27}$$

In the case of the pinned-free beam, the potential energy of the rotational spring is added to the system, and the stiffness matrix is given by

$$K_{ij} = \frac{1}{2}\int_0^L EI[z'']^2 dx + \frac{1}{2}\tau[z'(0)]^2 = \frac{1}{2}\int_0^L EI z''^T z'' dx + \frac{1}{2}\tau z'(0)^T z'(0) \tag{2-28}$$

Once the mass and stiffness matrices are formed for each boundary condition, the Rayleigh-Ritz method continues by defining the eigenvalue problem given by

$$\sum_{j=1}^{n} c_j\left(K_{ij} - \omega^2 M_{ij}\right) = 0 \tag{2-29}$$

where c_j contains the eigenvectors of the system and ω^2 contains the eigenvalues of the system. The square root of the eigenvalues gives the natural frequencies of the beam in $\frac{rad}{s}$ [31].

When calculating the natural frequency of a beam in air, the surrounding fluid properties are usually neglected since the air has little effect on the motion of the beam. However, when

calculating the natural frequency of a beam in a denser fluid, the mass of the surrounding fluid must be taken into account. Essentially, the mass of the surrounding fluid must be added to the vibrating structure. In the case of a circular cross section, the added mass per unit length is given by

$$A_{xx} = A_{yy} = \frac{\rho_{fluid}\pi L^2}{4} = \rho_{fluid}A(x) \tag{2-30}$$

where A_{xx} is the added mass per unit length for acceleration along the x-axis, A_{yy} is the added mass per unit length for acceleration along the y-axis, ρ_{fluid} is the density of the fluid surrounding the vibrating structure, L is the circular cross section diameter, and $A(x)$ is the cross section area at location *x* along the beam [32]. By including the added mass per unit length, the beam's total mass per unit length at location *x* along the beam is given by

$$m_{total}(x) = \left(\rho_{beam} + \rho_{fluid}\right)A(x) \tag{2-31}$$

where ρ_{beam} is the density of the beam. Therefore, when calculating the natural frequencies of a beam in a fluid other than air using the Rayleigh-Ritz method, the total density of the beam can be described by

$$\rho_{total} = \rho_{beam} + \rho_{fluid} \tag{2-32}$$

3 Experimental Methods

3.1 Artificial Inner Hair Cell

The biomimetic hair cell sensors described in this paper are an extension of earlier work in creating hair cell flow sensors using the regulated attachment method (RAM) [17-19]. The primary inspiration for the current hair cell sensor is the hair cell flow sensor presented by Sarles [19] that featured a bilayer formed between a hydrogel and an aqueous volume. In this work, a lipid bilayer is formed between two hydrogels, with one of the hydrogels acting as the root of an artificial hair. Both of the hydrogels lay in a flexible polyurethane (Clearflex 50, Smooth-On, Inc.) substrate at the bottom of connected elliptical wells, as shown in Figure 3-1. To allow for phospholipid self-assembly to occur, the wells are filled with hexadecane oil (Sigma-Aldrich).

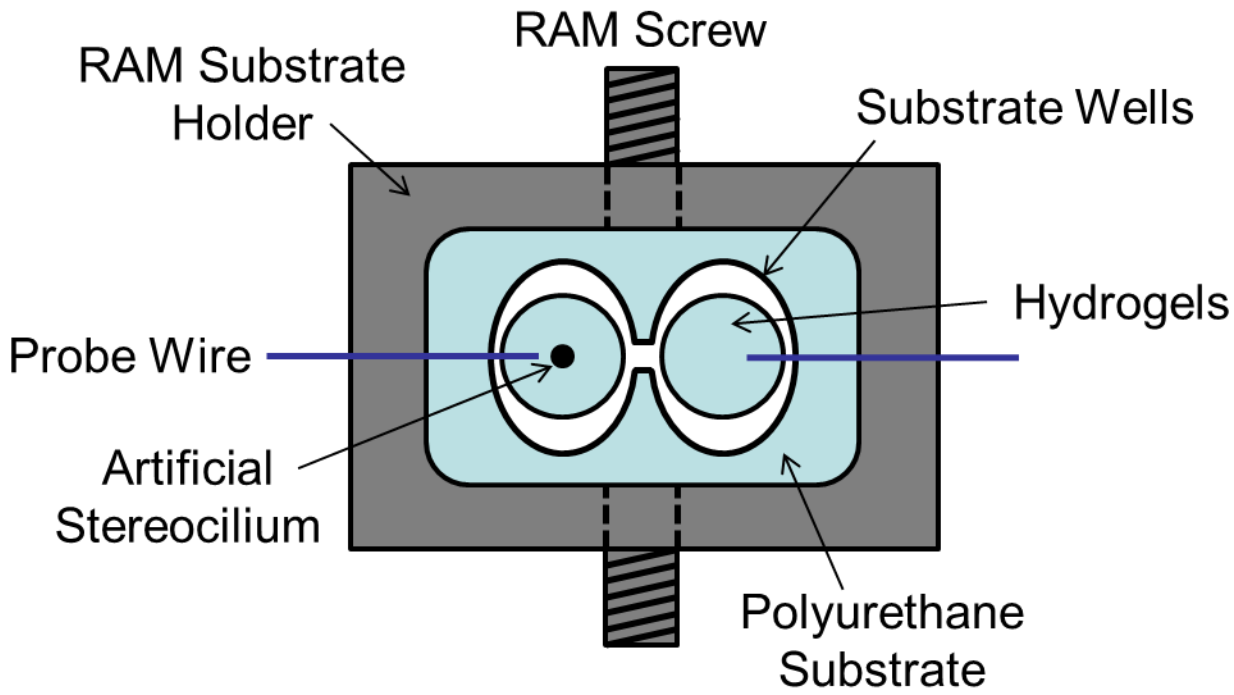

Figure 3-1. Top view of hair cell substrate, RAM substrate holder, and hydrogels. Tightening and loosening the RAM screws controls the size of the gap connecting the two elliptical wells.

Hydrogels are fabricated using a cylindrical polyurethane mold, shown in Figure 3-2, having a hole to direct the probe wire to the center of the hydrogel. Hydrogel solution, 80% (w/v) polyethylene glycol dimethacrylate (PEG-DMA, MW = 1000 g/mole, Polysciences, Inc.) in a pH 7 buffer solution containing 500 mM potassium chloride (KCl, Sigma Aldrich) and 10 mM 4-morpholinepropanesulfonic acid (MOPS, Sigma Aldrich), fills the mold and is then cured using a handheld ultraviolet (UV) light to form the solid hydrogels. When forming the hydrogel that acts as the root of the artificial hair, the hair is held in a vertical orientation during the curing process. The UV light positioning and steps used to cure the hydrogel are given in Table A-1. Tapered glass hairs, as opposed to the commercially available synthetic fibers used by Sarles [19], are used in these tests. A glass pipette puller is used to form the hairs and cause the tapered shape. The glass hair and hydrogel dimensions are listed in Figure A-2. Silver-silver chloride (Ag/AgCl) probe wires with a diameter of 125 μm are cured in the hydrogels and are the electrical leads of the AIHC.

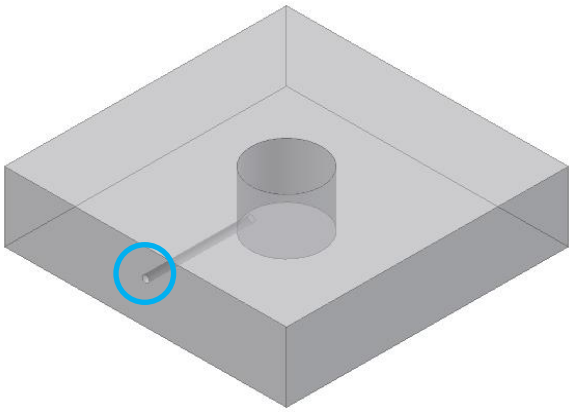

Figure 3-2. Model of the cylindrical polyurethane mold used to fabricate the hydrogels. The small hole circled in the image indicates the location of the hole used to direct the probe wire to the center of the hydrogel. Note that the probe wire hole in this figure is increased in diameter for visibility.

After the hydrogels have been fabricated with protruding electrical leads, the hydrogels are placed close together in the wells and the probe wires glued into place. Hexadecane oil is added to the wells and the substrate is glued into place in the RAM substrate holder. Figure 3-1 also shows a diagram of the RAM substrate holder, which allows the distance between the hydrogels to be actively manipulated by the user tightening or loosening the screws, thus facilitating monolayer and bilayer formation. The RAM process has been thoroughly described by Sarles [17]. The initial dimensions of the polyurethane substrate were varied until the RAM screws could reliably separate and join together the lipid droplets without deforming the soft hydrogels. The final set of substrate dimensions is given in Figure A-1.

After the substrate is attached to the RAM substrate holder and the wells filled with oil, a small amount of lipid solution is added between the hydrogels. The lipid solution is composed of 20% (w/v) diphytanoyl phosphocholine (DPhPC) phospholipid vesicles (Avanti Polar Lipids, Inc.) in a pH 7 buffer solution containing 500 mM KCl (Sigma) and 10 mM MOPS (Sigma). Figure 3-3 shows the three main steps in the modified RAM process. As shown in Figure 3-3a, the lipids are deposited on the inner surface of the hydrogels to facilitate attachment, forming a connection between the two electrical leads having very low resistance and only stray capacitance. In the second step of the RAM process, the hydrogels are separated and the lipids split into two sections, called droplets. Each droplet remains attached to a hydrogel. As the droplets are held apart for approximately 1 minute, lipid monolayers form on the outside of each droplet. The RAM screws are slowly loosened, allowing the droplets to come together and touch in the small gap connecting the elliptical substrate wells. This final step is shown in Figure 3-3c. The droplet contact is monitored from underneath the substrate through a microscope. Once the droplets contact each other, a bilayer slowly forms. A more thorough description of bilayer

formation is presented by Bayley [33]. The RAM process is repeated to test that a bilayer can be reliably formed before attaching the RAM substrate holder to the fluid channel for testing.

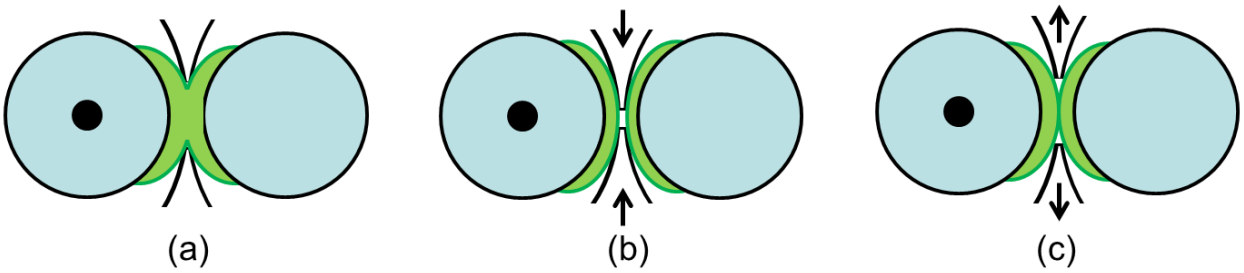

Figure 3-3. Diagram of the steps in the modified RAM used to form a bilayer in the AIHC. In step (a), lipid solution is deposited into the AIHC and attaches to each hydrogel. In step (b), the RAM screws are tightened to separate the lipid droplets. The RAM screws are slowly loosened to allow the droplets to touch and a bilayer to form in step (c).

3.2 Artificial Cochlear Environment

To recreate the cochlear environment around the AIHCs, a fluid channel capable of creating sinusoidal flows is created. Figure 3-4 shows a picture of the fully assembled artificial cochlear environment (ACE). The dimensions of the ACE are given in Figure A-3. A cutout for the hair cell substrate is located at the bottom of the channel while inlet and outlet fluid fill ports are located at the top and side of the channel. Three square flanges are attached to the substrate cutout and each end of the channel. The RAM substrate holder attaches to the bottom flange to hold the AIHC's artificial stereocilium in the middle of the fluid channel. Acrylic sheets and tubing were used for all parts of the ACE, and nylon nuts and bolts were used to attach the RAM substrate holder. Non-metal materials were chosen in the construction to reduce the amount of electrical noise in the system. A thin film of polyurethane (Clearflex 50, Smooth-On, Inc.) is permanently attached to each of the end flanges. A cork/rubber gasket is used in firmly attaching the RAM substrate holder to prevent fluid leakage. The polyurethane film on one end of the channel receives an external sinusoidal input, thus transmitting the force to the fluid and causing

sinusoidal fluid flow. Pressure relief is provided to the system by a vertical acrylic tube open to atmosphere. With the ACE fully assembly, the channel is filled with fluid through the inlet port. Since the top of the hair cell substrate is open to the fluid environment, hexadecane oil must be used to fill the channel.

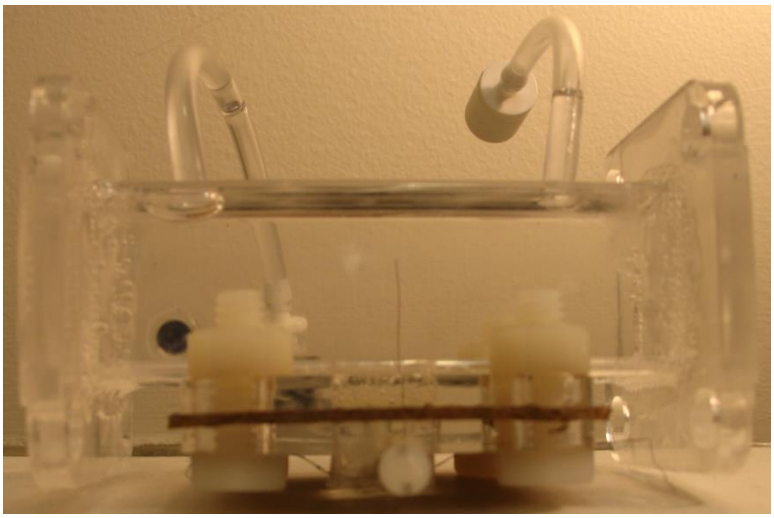

Figure 3-4. Picture of the assembled fluid channel modeling the cochlear environment. The RAM substrate holder is attached to the bottom of the channel. The vertical acrylic tube providing pressure relief to the system protrudes from the back of the ACE and is not visible in this view.

3.3 Biological Dynamic Similitude

One of the main considerations in designing the AIHC and ACE was the relationship between the biological case in the human cochlea and the artificial case developed in this paper. Using the Reynolds number and Womersley number to describe the flow around the stereocilium allowed for direct comparison between the biological and artificial cases. Dynamic similitude is the condition where the relationship of like forces between a real system and model are equated using proper parameter scaling [25]. Initially, a goal in the development of the AIHC and ACE was to design a system capable of producing a fluid flow with Reynolds and Womersley numbers matching the flow around the stereocilia in the human cochlea, thus achieving dynamic similitude. However, the use of a fluid velocity and stereocilium diameter on a biological-scale

would likely lead to stereocilium displacements so small that the AIHC would be unable to detect the fluid flow. Therefore, a compromise between biological similarity and AIHC effectiveness was made to increase the amount of force imparted by the fluid on the artificial stereocilium, with the primary goal of the project to mimic the transduction method used in the cochlear IHCs.

To increase the amount of force on the artificial stereocilium, the stereocilium diameter and fluid velocity were increased compared to the biological case. Additionally, the ACE's cross section was sized so that a long artificial stereocilium could be used to increase the surface area exposed to the fluid flow, thus increasing the force acting on the stereocilium. Table 3-1 lists the biological values for fluid flow in the human cochlea and the proposed values for the AIHC and ACE. The biological values were reported by Baumgart et al. and are characteristic of fluid flow around the stereocilia responding greatest to a driving frequency of 1000 Hz [34]. The proposed test setup values, except for the known kinematic viscosity of hexadecane oil, are estimates of what the final values would be after the AIHC and ACE were created.

Table 3-1. Reynolds number and Womersley number parameters for the biological case in the human cochlea and proposed test setup.

Parameter	**Biological Value**	**Proposed Test Setup Value**
Stereocilium Bundle Diameter (μm)	5	~200
Fluid Frequency (Hz)	1000	~80
Fluid Velocity (mm/s)	0.1	~5
Kinematic Viscosity (cSt)	1	3.935[35]
Reynold's Number	5E-4	~0.25
Womersley Number	0.4	~2.25

Using Equations (2-5) and (2-6), the Reynold's and Womersley numbers for the biological case and proposed test setup are listed at the bottom of Table 3-1. By increasing the stereocilium

diameter and fluid velocity without dramatically increasing the fluid kinematic viscosity, the Reynolds number for the proposed test setup is four orders of magnitude greater than the biological case. However, the use of a much lower fluid frequency led to more similarity between Womersley numbers. Although dynamic similitude could not be achieved due to the much higher Reynolds number, the proposed test setup seeks to test whether the AIHC can mimic the transduction mechanism in the human cochlea and sense the sinusoidal fluid flow in the ACE.

3.4 Experimental Setup

A diagram of the ACE setup is shown in Figure 3-5. The input into the ACE is the excitation force, which pushes and pulls the acrylic plug on the left side of Figure 3-5. As the excitation force displaces water in the ACE, the fluid level rises and falls in the pressure relief tube at the top of the fluid channel. The use of a pressure relief tube that is open to atmosphere prevents pressure buildup in the ACE, which would deform the polyurethane substrate and subsequently the size of the bilayer.

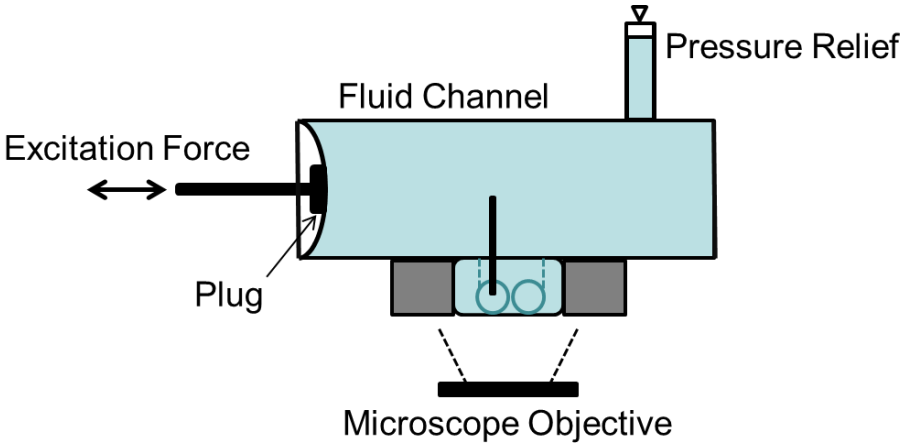

Figure 3-5. ACE setup diagram showing the fluid channel with RAM substrate holder and hair cell sensor attached. The modal shaker produces an excitation force which pushes and pulls the elastic film, creating a sinusoidal fluid flow in the channel.

To fully evaluate the characteristics of both the AIHC and the ACE, the testing setup diagram shown in Figure 3-6 is used. The single input into the system is the signal from the sine wave generator, which connects to a 4810 Bruel and Kjaer mini shaker. Input force and input plug velocity are monitored by the load cell and laser vibrometer and provide useful information when evaluating the characteristics of the ACE and AIHC. Plastic threaded rods connect the shaker to the load cell and the load cell to the acrylic plug on the ACE. The output of the system is the AIHC current, which is preprocessed by the Axopatch 200B lock-in amplifier and DigiData 1440A (Molecular Devices) to output a voltage. Load cell voltage, laser vibrometer voltage, and AIHC voltage data are collected by the DigiData 1440A data acquisition (DAQ) system.

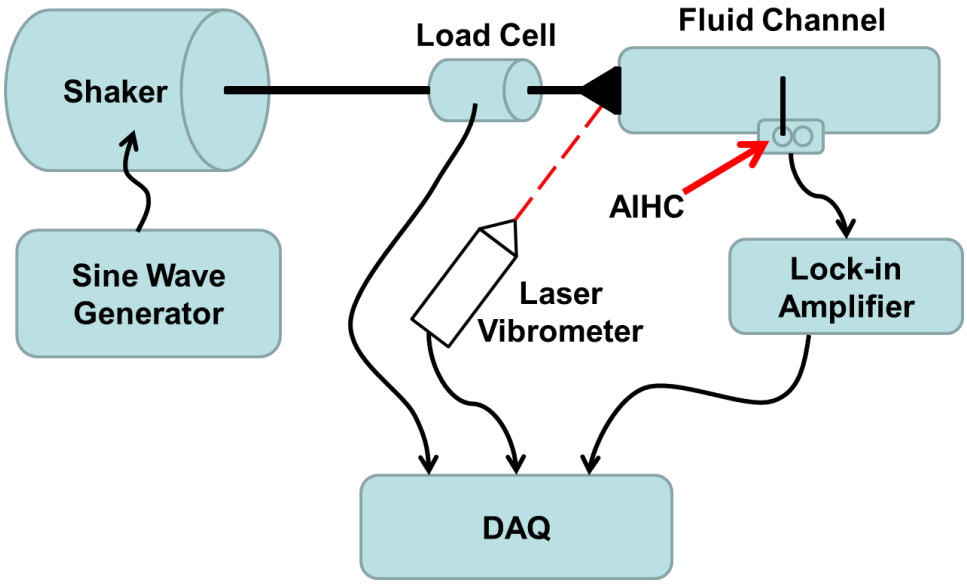

Figure 3-6. Diagram of the experimental setup showing the inputs and outputs of the system. The sine wave generator controls the shaker, which is attached through the load cell to the fluid channel by plastic rods. The load cell, laser vibrometer, and lock-in amplifier collect the system's output data, which is recorded by the DAQ.

Figure 3-7 displays an image of the experimental setup and more clearly shows the orientation of the ACE and shaker. The red and blue leads connect the AIHC probe wires to the Axopatch

headstage. Moldable clay holds the end flanges of the ACE firmly in place. The bright red dot indicates the measurement point of the laser vibrometer, which is not shown in the image.

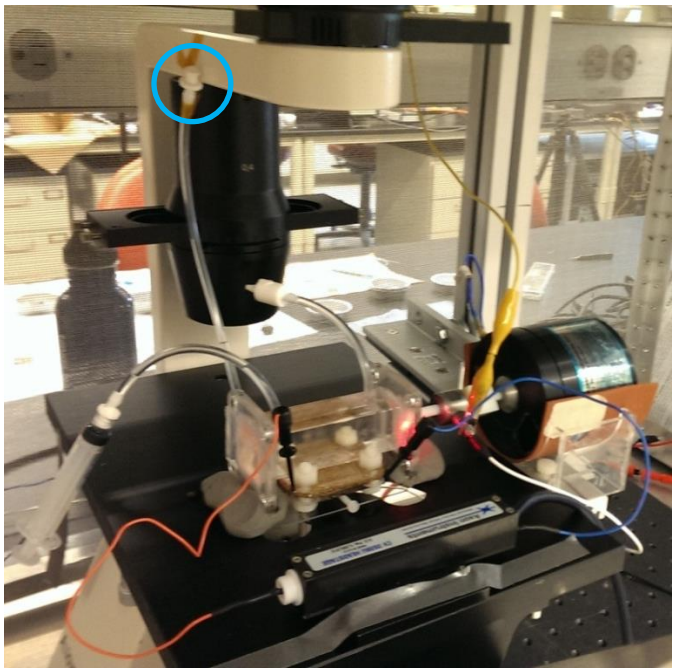

Figure 3-7. Picture of the experimental setup for characterizing the ACE and AIHC. The red and blue leads connect the AIHC positive and negative probe wires, respectively, to the Axopatch headstage. Pressure relief is provided by the vertical tube attached to the top of the microscope, circled in blue.

Not shown in Figure 3-7 is the laser vibrometer placement. The laser vibrometer must be placed off to the side of the test setup to have an unobstructed view of the input plug. The orientation of the laser vibrometer to the acrylic plug is indicated in Figure 3-8. The threaded rod connecting the load cell and the input plug has a cone-shaped end that meets the plug. A piece of retroreflective tape is placed on the cone-shaped end to allow the laser to be placed in different locations and still detect the reflected laser. If the surface was not covered in retroreflective tape, the laser would have to be pointed perpendicular to the cone-shaped end. Because the laser is not parallel to the input plug's movement, a scaling factor must be applied to the velocity

detected by the laser vibrometer to measure the input plug's velocity. The input plug velocity is given by

$$V_{plug} = V_{LV} \frac{a}{\sqrt{a^2 + b^2}} \tag{3-1}$$

where V_{plug} is the velocity of the input plug, V_{LV} is the velocity measured by the laser vibrometer, and *a* and *b* are the dimensions indicated in Figure 3-8.

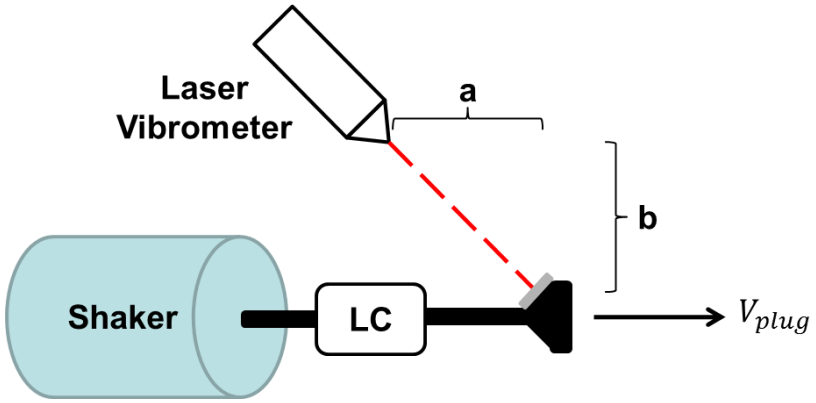

Figure 3-8. Top view of the laser vibrometer orientation to the acrylic plug at the input to the ACE. The laser vibrometer is positioned with dimensions *a* and *b* approximately equal. A small piece of retroreflective tape, shown in gray, is placed on the cone-shaped plastic piece connecting the load cell to the input plug.

3.5 Testing Procedures

The testing procedures described in this section all start with the experimental setup described in Section 3.4. The placement and orientation of the equipment shown in Figure 3-7 must be carefully setup to ensure consistent testing conditions and repeatable results. Aluminum shielding is wrapped around the shaker and load cell and grounded to the faraday cage that surrounds the entire setup. The aluminum shielding and faraday cage greatly reduce the amount of 60 Hz electrical noise in the AIHC current measurements. Additionally, all of the metal components of the microscope are grounded. Because no noticeable increase in electrical noise

was seen in the test data, the front of the faraday cage was removed to allow for an unobstructed line of sight for the laser vibrometer.

Before the actual test begins, a preliminary test is run to ensure that the physical movement of the shaker is not detected by Axopatch headstage. A bilayer is then formed using the modified RAM method described in Section 3.1. The bilayer formation is verified by applying a triangle wave across the bilayer. The resulting square wave output of the AIHC is then recorded. The final preliminary test measures the noise level when no triangle wave is applied to the bilayer and no external force is applied to the ACE. This test indicates the amount of outside noise that will be present during the actual tests. Once the system has been properly shielded from electrical noise and the physical shaker movement, the actual tests can begin.

3.5.1 Frequency Tuning Tests

The frequency tuning tests presented in this work consist of a series of tests all measuring the response of the AIHC or a control case to a frequency sweep sinusoidal input from the shaker. The chirp signal used in these tests is a linear sweep from 1-400 Hz, taking 30 s per sweep, and repeated a total of four times. The chirp signal is output from the function generator to the shaker and has constant amplitude. For some of these tests, the DC offset applied across the AIHC's bilayer is also changed.

The first frequency tuning test compares the response of the AIHC to a control case where the artificial stereocilium has been removed from the AIHC. This test seeks to determine whether or not the artificial stereocilium is acting as part of the sensor's transduction mechanism. This test is carried out by applying the chirp signal mentioned above to the ACE with both the AIHC and the AIHC lacking an artificial stereocilium. DC offset across the bilayer and input force are kept

constant. If the response of the AIHC and the control case are similar, it is unlikely that the artificial stereocilium plays a role in current generation in the AIHC. A breakdown of the constant and variable parameters used in the testing procedures is listed in Figure 3-9.

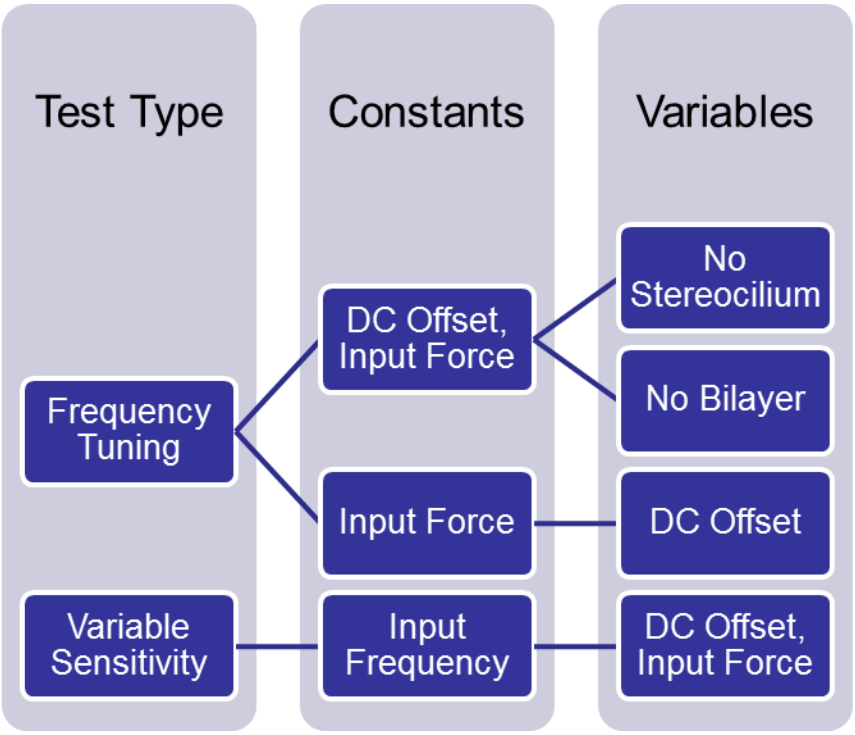

Figure 3-9. Diagram of the parameters used in the AIHC characterization tests. A chirp signal input is used for all of the frequency tuning tests while a constant frequency input is used for the variable sensitivity tests.

Another control test is performed in the ACE and tests whether or not the presence of the bilayer is essential to current generation in the AIHC. DC offset and input force are again kept constant, and the same chirp signal is used from above. However, the control case in this second test features an AIHC without a bilayer. The lipids are separated to remove the bilayer, leaving a purely resistive connection between the two hydrogels. Comparing the responses of the AIHC and the control case lacking a bilayer will show if the bilayer is critical to the function of the AIHC, or if current is being generated by some other means.

The final frequency tuning experiment involves testing the AIHC at a variety of DC offsets. For each of these tests, the chirp signal from the previous tests is kept the same. However, the DC offset is changed between tests. The DC offset is increased until the potential level where the lipids coalesce. By conducting this third frequency tuning test, how the AIHC responds to a range of driving frequencies at various DC offsets can be evaluated. Of particular importance is determining if the AIHC has a peak output at a certain driving frequency and if the peak output increases with DC offset.

3.5.2 Variable Sensitivity Tests

Beyond characterizing the ACE and AIHC, the last research objective of this work is mimicking the variable sensitivity found in the cochlea, as discussed previously in Section 1.1. For these tests, a sinusoidal wave of constant frequency is applied to the shaker. During this series of tests, the input force and DC offset are varied. Changing the input force tests how the AIHC responds to fluid flows of different velocities. In addition to characterizing the AIHC, these tests also indicate how well the fluid velocity in the ACE can be controlled. At the conclusion of the variable sensitivity tests, the goal of this work is to determine what level of DC offset is needed at each input force to imitate the nonlinear gain found in the human cochlea.

3.6 Data Analysis

This section will discuss the types of data collected in the previously mentioned steps and how the raw data is processed and analyzed. The data collected from all of the tests consist of measurements of the input and output. The input into the system can be quantified in three ways: the input force being applied to the input plug on the ACE, the input velocity of the input plug, and the fluid velocity around the AIHC's artificial stereocilium. An Axopatch 200B patch-clamp

amplifier and a DigiData 1440A digitizer are used to collect the current data from the AIHC. These current measurements are the output of the system.

3.6.1 Averaging Time Domain Data

Because of the small magnitude of the input and output data, noise reduction became a priority in processing the raw data. Averaging the data in the time domain caused a reduction in the noise level while maintaining the signal of interest. To average the data in the time domain, the responses to each of the four frequency sweeps mentioned in Section 3.5.1 are averaged. Figure 3-10 shows the effect of averaging hair cell current data in the time domain. Figure 3-10a shows an example response of the hair cell current to one frequency sweep. When the hair cell current response is averaged over the four frequency sweeps, the plot in Figure 3-10b is obtained. By averaging the response, the noise level is reduced while the peak in the signal around 6 s is not greatly affected.

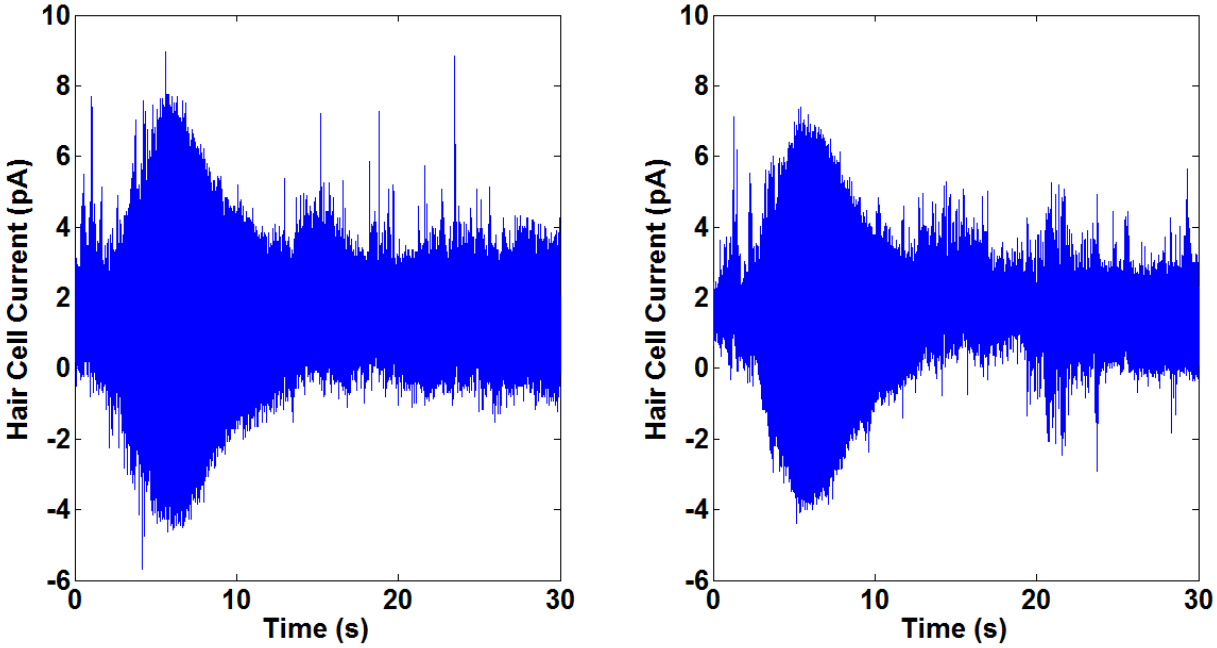

Figure 3-10. Effect of averaging hair cell current data in the time domain when the AIHC is subjected to a chirp signal. (a) shows the response of the AIHC to one frequency sweep. (b) shows the time domain averaged response of the AIHC to four frequency sweeps. The averaged response shows less overall noise without a considerable reduction in the peak of the hair cell current.

Figure 3-10 is just one example of hair cell current data. Similar effects on noise levels are seen when the input force and velocity are averaged over the four frequency sweeps. After the noise level is reduced by time domain averaging, the next step in the analysis process depends on the type of test. Since the variable sensitivity tests were all conducted at the same frequency, analysis in the time domain gives the most useful information about the data. In the variable sensitivity tests, a band-pass filter with a center frequency equal to the driving frequency is applied to the time domain data. The analysis is completed by calculating the root mean square (RMS) of the filtered data.

3.6.2 Frequency Domain Analysis

The frequency tuning tests require a more involved analysis to accurately interpret the data. The most important question encountered in analyzing the frequency tuning data was how to quantify the relationship between the input and output of the AIHC. Cross power spectral density (CPSD) analysis allows the input and output to be directly related in the frequency domain. Primary analysis in the frequency domain was critical for quantifying the response of the AIHC at particular frequencies.

The correct use of windowing functions is imperative when trying to extract useful information from a CPSD plot [36]. Windowing functions are used to reduce the amount of noise in a CPSD plot. An example of the effect of windowing is displayed in Figure 3-11. The dark blue line shows the results of a CPSD analysis between an example hair cell current output and the ACE plug velocity input with no windowing used. It is important to note that the CPSD input for the example data is not the same as the results data discussed in Section 4.2. The use of an insufficient number of windows, in this case 8 and 40 windows, actually leads to a less accurate representation of the CPSD. Only when the number of windows is increased to 72 does the plot become legible. This example analysis, as well as further analysis on the data, led to the use of 72 windows in the analysis of the frequency tuning tests.

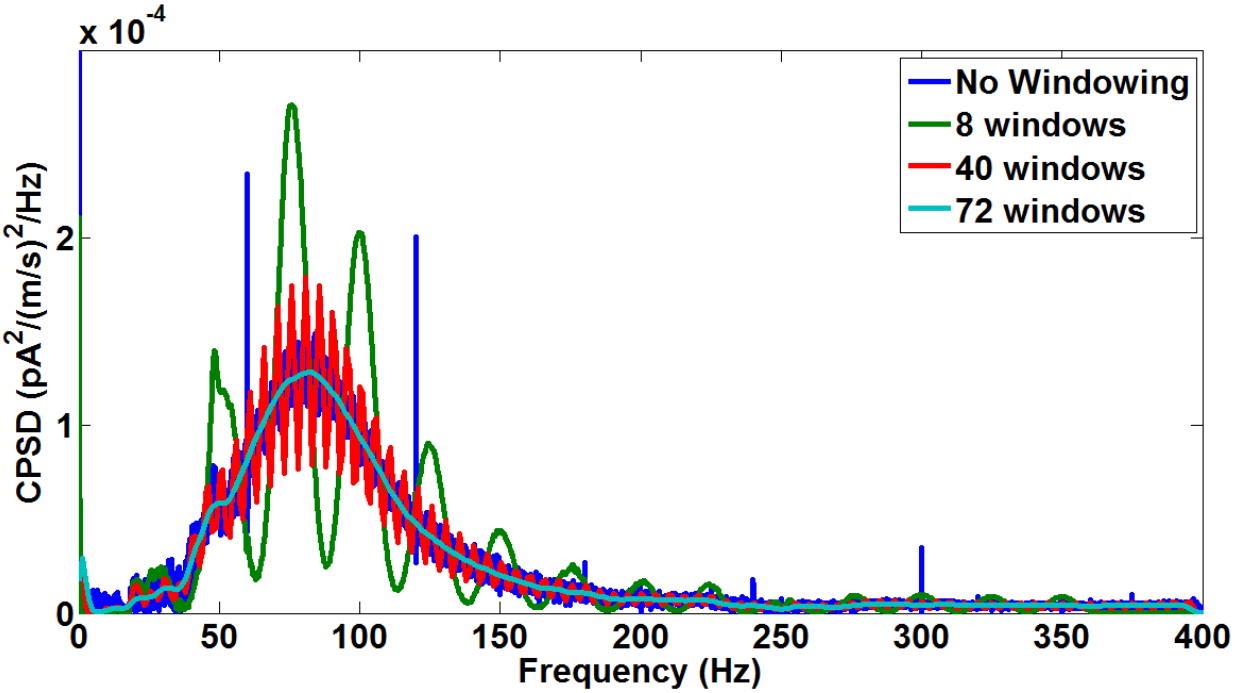

Figure 3-11. Effect of number of windows on the cross power spectral density between input plug velocity and output hair cell current. Blackman-Harris windowing functions with 50 percent overlap are applied to the cases with windowing. Similar results are seen with the use of different windowing functions.

Window type is also an important consideration when performing a CPSD. Different window types lead to different effects on the noise and signal within the data. Figure 3-12 presents the result of changing the window type on the same example data used in Figure 3-11. 72 windows with 50 percent overlap are used in the example plot in Figure 3-12. Except for the case of the rectangular windowing function, the window type does not appear to significantly change the resulting plot when a large number of windows is used. The final windowing function parameters used in analyzing the frequency tuning tests is 72 Blackman-Harris windows with 50 percent overlap.

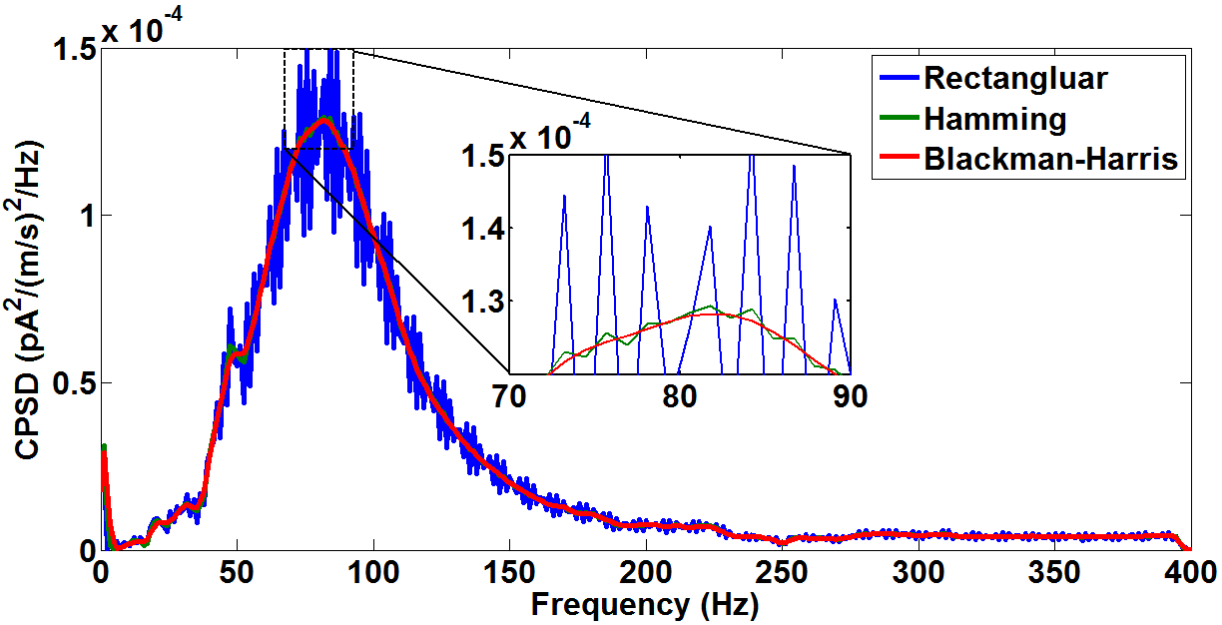

Figure 3-12. Effect of window type on the cross power spectral density between input plug velocity and output hair cell current, when applying 72 windows with 50 percent overlap. The small difference between the Hamming and Blackman-Harris windowing functions is shown in the inner plot.

The CPSD analysis of the frequency tuning tests is performed using Welch's method in MATLAB®. When applying windowing functions with the goal of determining the amplitude of a deterministic signal from a CPSD plot, a scaling factor must be used [36]. Without the scaling factor, the peak of a deterministic signal will change as the number of windows changes. However, the peaks in the frequency tuning test results do not show up as deterministic signals. Because the damping in the fluid system results in smooth peaks and slow roll offs in the CPSD plots, the peaks are seen as a type of "noise" in the data. These non-sharp peaks can be seen more closely in the Hamming and Blackman-Harris window examples in the inner plot of Figure 3-12. The aforementioned scaling factor is therefore not applied to the frequency tuning data analyzed using Welch's method.

Along with the CPSD, an analysis of the corresponding coherence can help determine the amount of noise in the input and output signals. The nondimensional coherence value always

falls between 0 and 1, with a value of 0 indicating that the input and output signals are entirely noise and a value of 1 indicating that there is no noise in the signals [37]. For the results presented in Section 4.2, the coherence is used to determine if the output signal is a result of noise in the system or a response to the input signal. Coherence values above 0.75 are considered good correlation between the input fluid velocity and output AIHC current.

The use of a CPSD allows the peak response frequency to be directly read from the CPSD plot. This information determines if the characteristics of the AIHC cause it to produce a larger output at a certain frequency or frequency range. Another important piece of information that can be extracted from the CPSD plots is the broadband power of the AIHC. Broadband power indicates the total power of the signal over a defined frequency range. In the case of the frequency tuning tests, CPSD data is integrated from 25 to 400 Hz to obtain the broadband power. The frequency range for the power integration is limited by the shaker characteristics and the frequency range of the input signal. Since the shaker creates inconsistent sinusoidal waves below 25 Hz, those frequencies were excluded from the power integration. Frequencies above 400 Hz were also excluded from the integration because 400 Hz is highest frequency in the input chirp signal.

4 Results

4.1 Artificial Cochlear Environment Flow Characteristics

A number of nondimensional parameters are used to characterize the fluid flow inside the ACE. The Reynolds number and Womersley number are used to quantify the level of biological similarity between the fluid flow driving the AIHC and the fluid flow found in the human cochlea. The combination of Keulegan-Carpenter number and frequency parameter determines if nonlinearities are occurring around the stereocilium. These nondimensional parameters are further discussed in Section 2.2.1. The results discussed in this section correspond to the fluid flows found in the frequency tuning tests from Section 3.5.1.

4.1.1 Nonlinearity Assumptions

The Keulegan-Carpenter number is plotted in the time domain as a function of frequency in Figure 4-1. The Keulegan-Carpenter number, as well as the rest of the parameters in Section 4.1, is displayed as a function of frequency because the chirp signal in the frequency tuning tests is a linear frequency sweep. Therefore, each frequency corresponds to a certain time, with 1 Hz occurring at 0 s and 400 Hz occurring at 30 s. The sinusoidal waves appear inconsistent below 25 Hz. This characteristic of the ACE can be attributed to the dynamics of the shaker. The shaker specification sheet does not detail its behavior below 25 Hz, indicating that the shaker may not be designed to operate at such low frequencies [38]. Therefore, the results below 25 Hz given in this section may not be an accurate representation of the fluid flow characteristics at higher frequencies in the ACE and can be ignored.

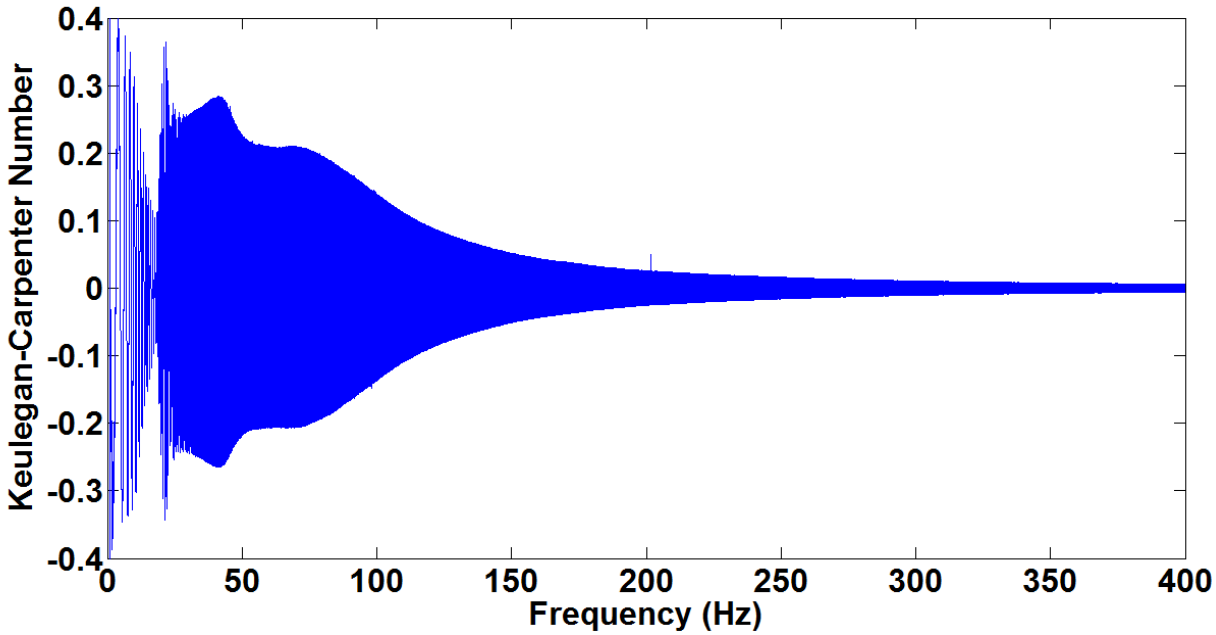

Figure 4-1. Keulegan-Carpenter number as a function of input frequency. This data is representative of the flow characteristics around the artificial stereocilium in the frequency tuning tests. Positive values indicate a Keulegan-Carpenter number where fluid flows away from the inlet. Negative values indicate fluid flow in the opposite direction, towards the inlet.

Ignoring the fluid flow below 25 Hz, the Keulegan-Carpenter number remains under 0.3 for the entirety of the frequency sweep used in the frequency tuning tests. Figure 4-2 shows the frequency parameter as a function of frequency for the frequency tuning tests. The combination of Keulegan-Carpenter number and frequency parameter determines if a symmetric flow field is present. The maximum value of the frequency parameter is 4.569, occurring at 400 Hz. Even if the maximum values for the Keulegan-Carpenter number and frequency parameter were to occur at the same frequency, they are both low enough (<10) to indicate that the flow field around the stereocilium is symmetric. Thus, no nonlinearities are present in the flow field.

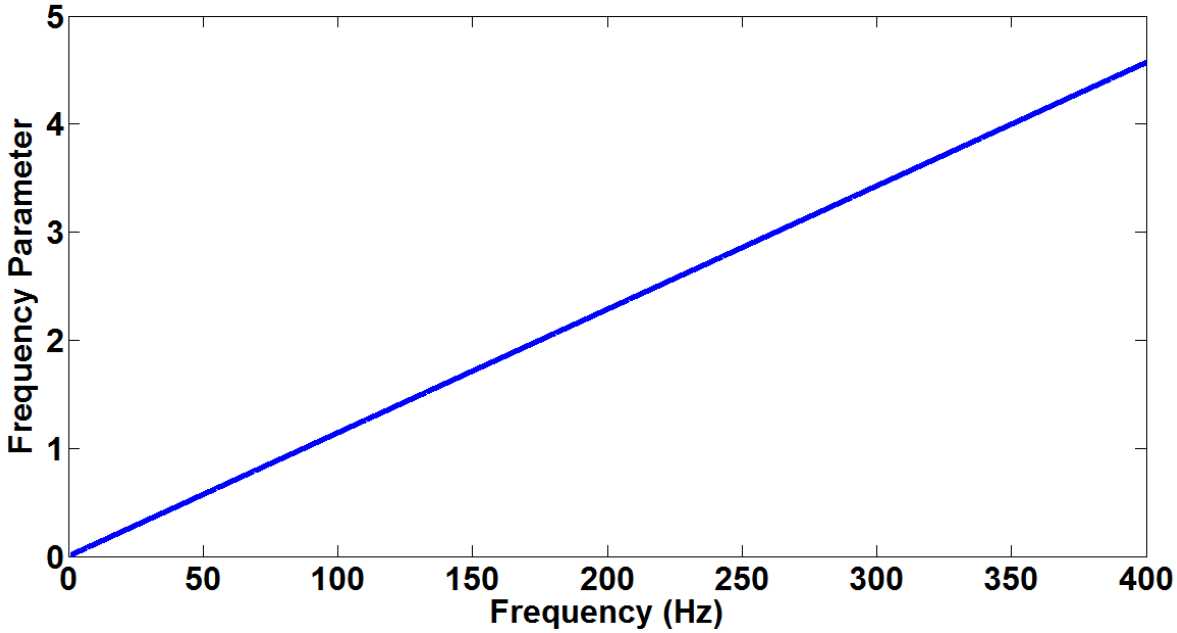

Figure 4-2. Frequency parameter as a function of input frequency. This data is representative of the flow characteristics around the artificial stereocilium in the frequency tuning tests.

4.1.2 Fluid Flow around the Artificial Stereocilium

The fluid flow around the artificial stereocilium of the AIHC is determined through a series of calculations and assumption checks. The first calculation is the volume velocity at the entrance of the duct. Applying Equation (2-9) to the input plug diameter given in Figure A-3 gives the volume velocity in the ACE. Solving for $\widetilde{w}$ in Equation (2-10) gives the shape of the velocity profile, which is independent of the volume velocity. The MATLAB® code used to solve for the velocity profile is given in Appendix B.1. Figure 4-3 shows the maximum velocity profile for three values in the frequency range used in the frequency tuning tests, 1, 25, and 400 Hz. The maximum velocity profile for each of these frequencies occurs at $t = T/4$, where T is the period of the sinusoidal flow. The velocity profile for each of the three cases in Figure 4-3 is fairly even. For a driving frequency of 1 Hz, there is some small variation in the fluid velocity near the edges of the duct. From Section 4.1.1, only frequencies above 25 Hz are relevant in the

evaluation of the ACE and AIHC. In this frequency range, the velocity profile can be assumed even.

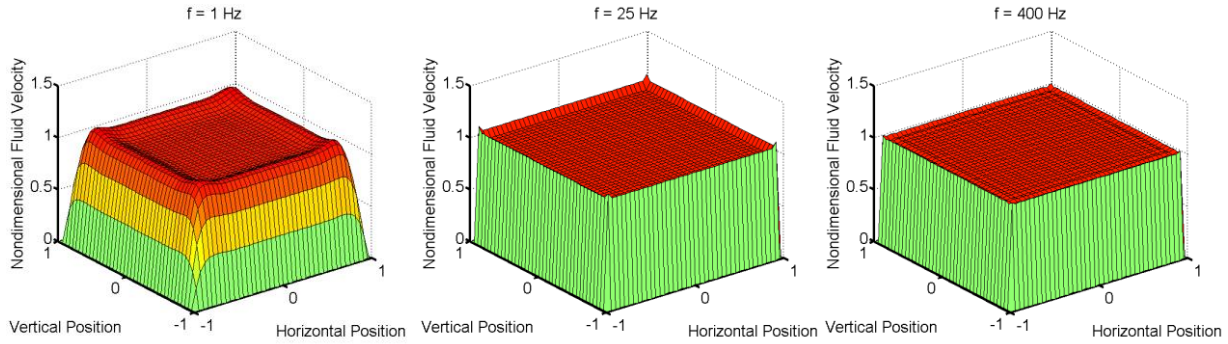

(a) (b) (c)

Figure 4-3. Maximum velocity profile in the ACE at three driving frequencies. The maximum velocity profile occurs at $t = T/4$ for each of these cases. The nondimensional fluid velocity, horizontal position, and vertical position are given by $\widetilde{w}$, ξ, and ζ from Section 2.2.2, respectively. (a), (b), and (c) show the velocity profiles for 1, 25, and 400 Hz, respectively. Velocity is fairly constant across the duct cross section, especially at 25 and 400 Hz.

When determining if the velocity profiles displayed in Figure 4-3 are fully developed near the artificial stereocilium, the entrance length assumption must be checked. When calculating the longest entrance length, using the maximum plug velocity from all of the performed tests of 0.021 m/s is necessary. Assuming an even velocity profile, as is the case for driving frequencies above 25 Hz, allows the use of Equation (2-17) in solving for the fluid velocity. Using Equation (2-5) to solve for the Reynolds number, the entrance length is calculated using Equation (2-16). The entrance length for the case of the maximum plug velocity is 0.893 mm. For lower plug velocities, the entrance length would be even shorter. With an entrance length much smaller than the distance from the duct entrance to the artificial stereocilium of 38.1 mm, the assumption of fully-developed oscillatory flow acting on the stereocilium is confirmed.

4.1.3 Biological Dynamic Similitude

The Reynolds number and Womersley number are used to determine how closely the AIHC and ACE model the dynamics of the biological system. Figure 4-4 displays the Reynolds number for the fluid flow around the stereocilium from the frequency tuning tests. The Reynolds number is plotted in the time domain as a function of frequency. The average diameter of the tapered glass hair is used in the Reynolds number calculation in Equation (2-5). The maximum Reynolds number around the artificial stereocilium is 0.1797, which occurs at a frequency of 78.88 Hz. The Womersley number in the frequency tuning tests is given in Figure 4-5. The Womersley number at an input frequency of 78.88 Hz is 2.379. Higher Womersley numbers are seen in the frequency tuning tests, as shown in Figure 4-5, but the only frequency of interest in analyzing biological dynamic similarity is the frequency producing the highest Reynolds number.

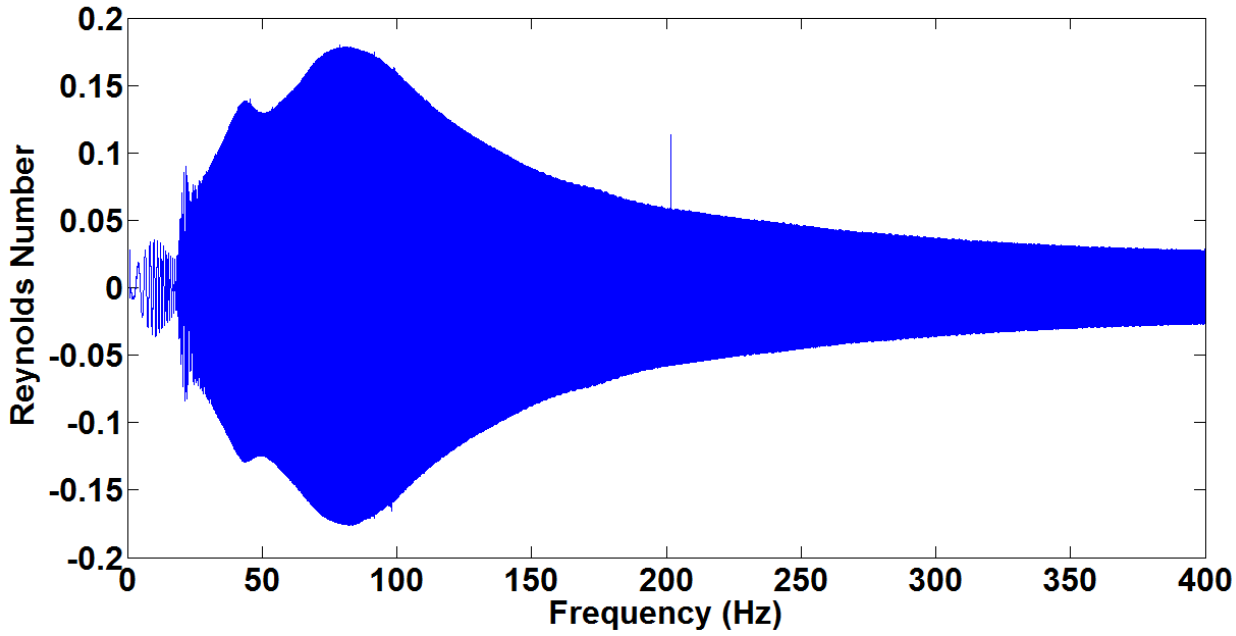

Figure 4-4. Reynolds number as a function of input frequency. This data is representative of the flow characteristics around the artificial stereocilium in the frequency tuning tests. Positive values indicate a Reynolds number where fluid flows away from the inlet. Negative values indicate fluid flow in the opposite direction, towards the inlet.

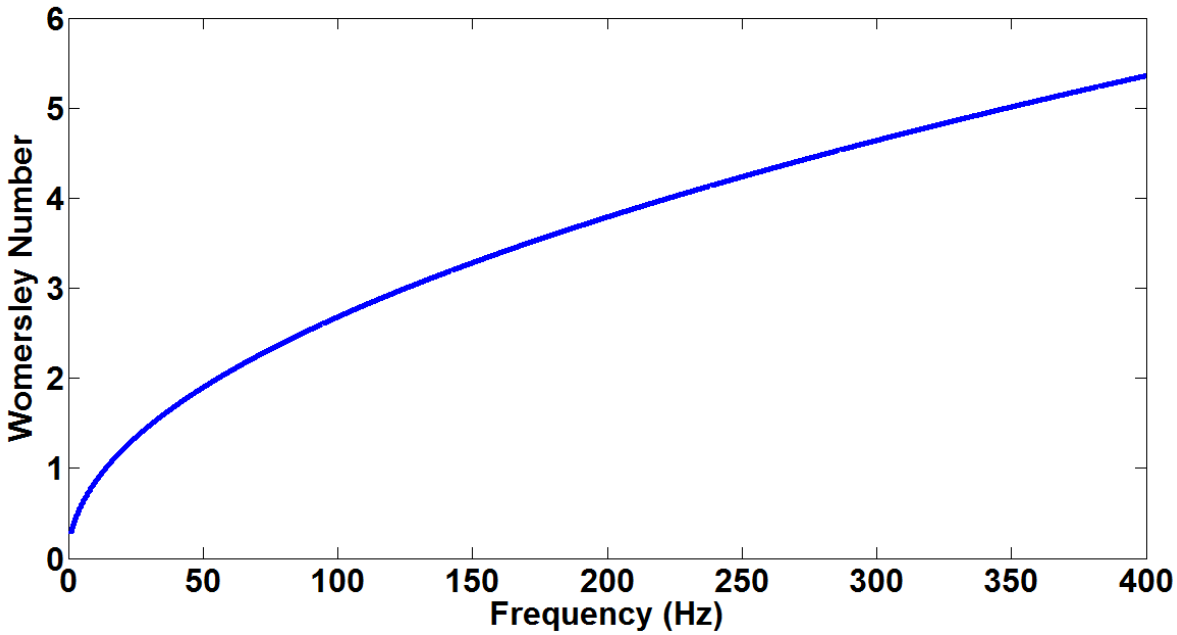

Figure 4-5. Womersley number as a function of input frequency. This data is representative of the flow characteristics around the stereocilium in the frequency tuning tests.

A summary of the Reynolds number and Womersley number parameters in the biological and AIHC cases is given in Table 4-1. Two AIHC cases are shown in Table 4-1, representing the maximum and minimum Reynolds numbers. The maximum AIHC case corresponds to the maximum Reynolds number that is found during testing. The minimum AIHC case is the theoretical minimum Reynolds number that could be achieved, corresponding to a fluid frequency of 400 Hz and a modal shaker input voltage of 1 V. The fluid velocity given for the minimum AIHC case includes a theoretical reduction in the fluid velocity corresponding to a modal shaker input voltage reduction from 10 V to 1 V. This theoretical reduction in fluid velocity is calculated by comparing the fluid velocities of the modal shaker voltage at 10 V and 1 V, which is visually displayed in Figure 4-15. The stereocilium diameter reported is the average diameter of the artificial glass stereocilium, whose dimensions are given in Figure A-2.

The Reynolds number in the maximum AIHC case is three orders of magnitude larger than the biological case. However, the Reynolds number is still low, indicating that viscous effects are dominant in the fluid flow around the stereocilium. The Womersley number for the maximum AIHC case, on the other hand, is on the same order of magnitude as the biological case. The relative similarity of the Womersley numbers indicates that both the artificial and biological cases have similar ratios of transient inertial forces and shear forces in the oscillatory flow. In the minimum AIHC case, both the Reynolds and Womersley numbers are one order of magnitude larger than the biological case. Although biological dynamic similitude is not achieved in the AIHC, the Reynolds number and Womersley number magnitudes prove that the AIHC fluid flow characteristics are similar to those found in the human cochlea.

Table 4-1. Reynolds number and Womersley number parameters for the biological case in the human cochlea and for two AIHC cases. The AIHC stereocilium diameter is the average diameter of the tapered glass hair. The maximum AIHC case fluid frequency indicates the frequency at which the maximum fluid velocity is achieved. The minimum AIHC case fluid frequency indicates the frequency where the minimum fluid velocity would be found, and includes a theoretical fluid velocity reduction corresponding to a modal shaker voltage reduction from 10 V to 1 V.

Parameter	**Biological Value**	**AIHC Value (max)**	**AIHC Value (min)**
Stereocilium Bundle Diameter (μm)	5	212	212
Fluid Frequency (Hz)	1000	78.88	400
Fluid Velocity (mm/s)	0.1	3.336	0.1411
Kinematic Viscosity (cSt)	1	3.935[35]	3.935[35]
Reynolds Number	5E-4	0.1797	7.6E-3
Womersley Number	0.4	2.379	5.357

4.2 Frequency Tuning Tests

The frequency tuning test discussed in this section detail how the AIHC responds to different variables. Tests comparing the AIHC to two control cases are carried out first to describe the

transduction mechanism of the AIHC with 0 mV DC offset applied across the AIHC bilayer. In each of the tests described in this section, a chirp signal from 1 to 400 Hz is sent into the ACE. The first control test compares the AIHC to an AIHC lacking a stereocilium. The second control test compares the AIHC to an AIHC lacking a bilayer. After the AIHC is characterized at 0 mV DC offset, the DC offset is increased to measure the changes in the AIHC response. Data analysis is performed in the frequency domain, using CPSD and coherence plots. Additionally, a transfer function estimate is computed comparing the input fluid velocity to the AIHC current output.

The same bilayer is used for each frequency tuning test that is not a control case. Because of its capacitive nature, sending a triangle voltage wave across the bilayer is used to determine its electrical properties. Using a normalized capacitance of 0.6 $\mu F/cm^2$, the capacitance of the non-control case bilayer used in these tests is 430.5 pF. This capacitance corresponds to a bilayer area of 71750 μm^2 [20].

4.2.1 Control Test 1: Stereocilium vs No Stereocilium

Figure 4-6 shows the CPSD of the response of the AIHC and the control case lacking an artificial stereocilium. The response labeled "Stereocilium" is the AIHC with 0 mV DC offset applied across its bilayer. 0 mV DC offset is also applied across the control case. The AIHC CPSD has major peaks at 60 Hz and approximately 75 Hz. The sharp peak at 60 Hz indicates that it is likely due to electrical noise in the system. The peak at 75 Hz is much smoother, with slower roll offs, indicating that it is likely the resonant frequency of the AIHC. The smooth roll offs are characteristic of a damped natural frequency that would be present in the response of an artificial stereocilium in a fluid channel. The control case lacking a stereocilium shows much lower amplitudes in the CPSD. Because the same fluid velocity is observed in the inputs for both the

AIHC and the control case, the lower CPSD response of the control case indicates that considerably less current is produced by the AIHC lacking a stereocilium. Without the artificial stereocilium, the fluid velocity seems unable to impart a significant force on the hydrogels and bilayer, thus decreasing the current output by a large amount. However, a peak does exist in the control case CPSD data at approximately 75 Hz. This peak, just like the peak in the AIHC data, suggests damped dynamics. Therefore, it cannot be concluded that the fluid in the ACE has no impact on the hydrogels, even without an artificial stereocilium present in the AIHC. The effect of fluid flow acting directly on the hydrogels, however, is very low and can be neglected when a stereocilium is present.

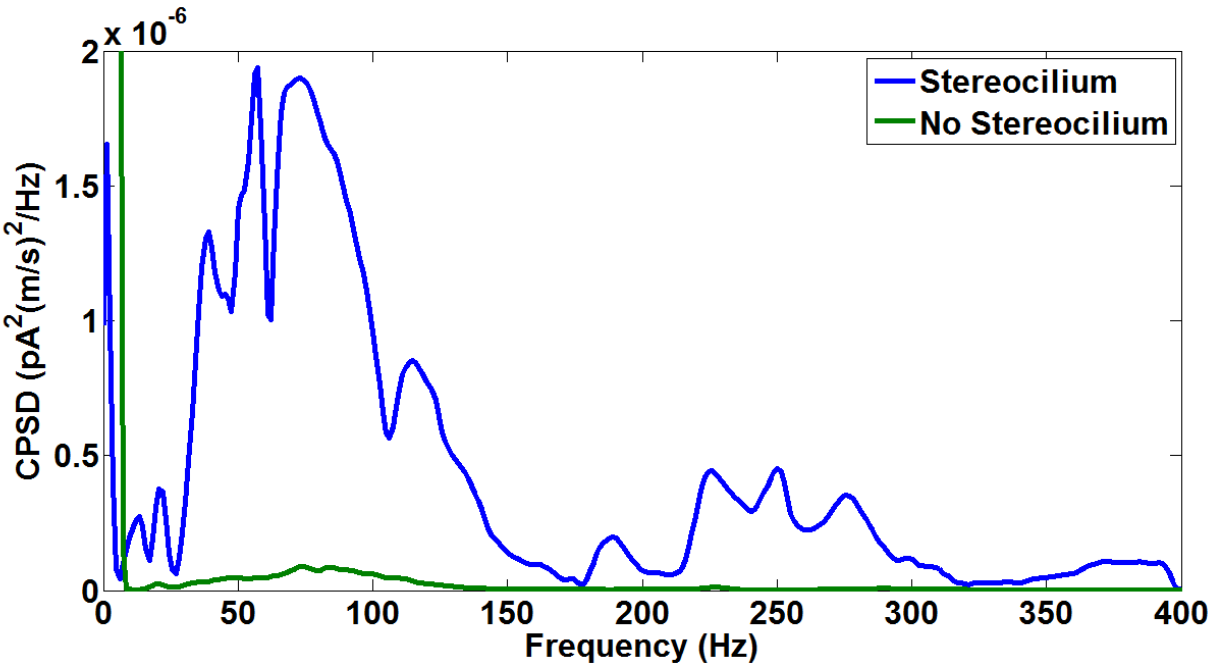

Figure 4-6. Cross-spectral power as a function of frequency of the AIHC and AIHC lacking an artificial stereocilium. The input to the ACE is a chirp signal with a linear frequency sweep from 1 to 400 Hz, repeated 4 times. The fluid velocity around the stereocilium and the AIHC current act as the input and output components, respectively, of the cross power spectrum. The AIHC and AIHC lacking a stereocilium both have 0 mV DC offset applied across their bilayers.

The coherence plot corresponding to Figure 4-6 is shown in Figure 4-7. Overall, the coherence for both cases are similar and poor across the frequency range. However, for the frequency range where the CPSD output is highest, 60 to 120 Hz, the coherence of both cases is above 0.75. As discussed in Section 3.6.1, coherence above 0.75 indicates low noise in the measurements and good correlation between AIHC input and output. Good coherence shows that the input fluid velocity is probably the cause of the current output, in both the AIHC and control case. Therefore, it can be concluded that the current setup of the AIHC does not keep fluid flow from generating current, although the artificial stereocilium increases current output by over 20 fold at 0 mV DC offset.

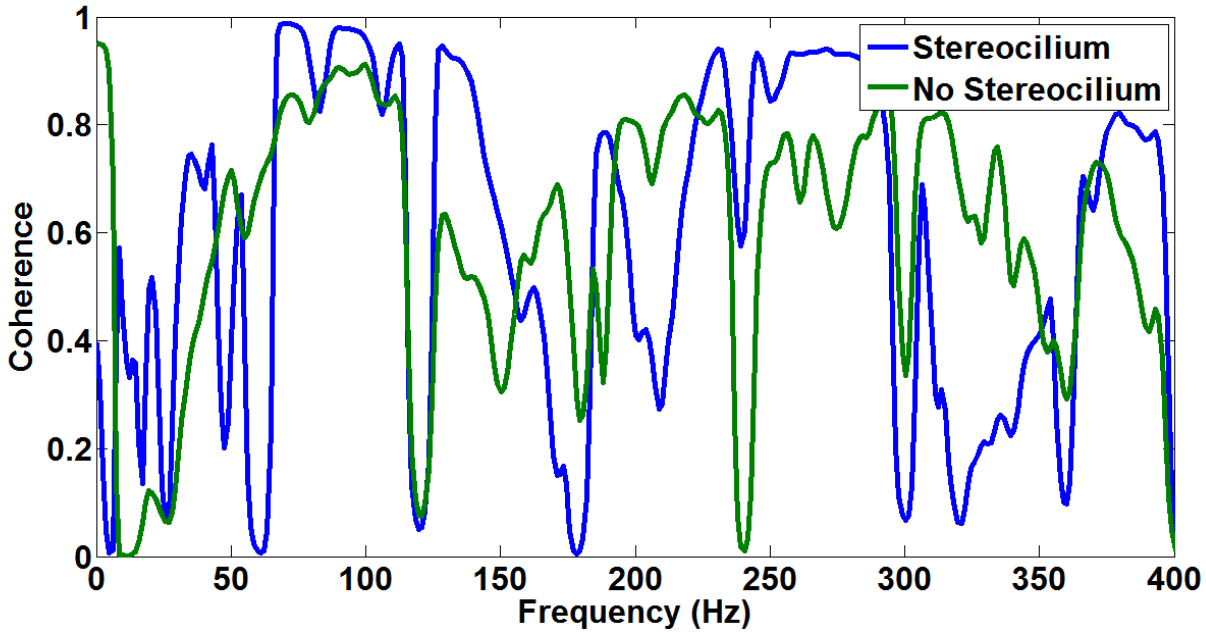

Figure 4-7. Coherence of the CPSD comparing the AIHC and AIHC lacking a stereocilium. The corresponding CPSD is shown in Figure 4-6. Of particular importance is the coherence of each case where the frequency response is highest, between 60 and 120 Hz.

4.2.2 Control Test 2: Bilayer vs No Bilayer

Figure 4-8 displays the CPSD plot of the AIHC compared to the control case lacking a bilayer. Both cases show similar CPSD results with peaks at approximately the same frequencies. The AIHC results, labeled "Bilayer" in Figure 4-8, are the same data set in Section 4.2.1. With peaks of the same magnitude at approximately the same frequencies, the presence of a bilayer seems to make little difference in the AIHC current output at 0 mV DC offset.

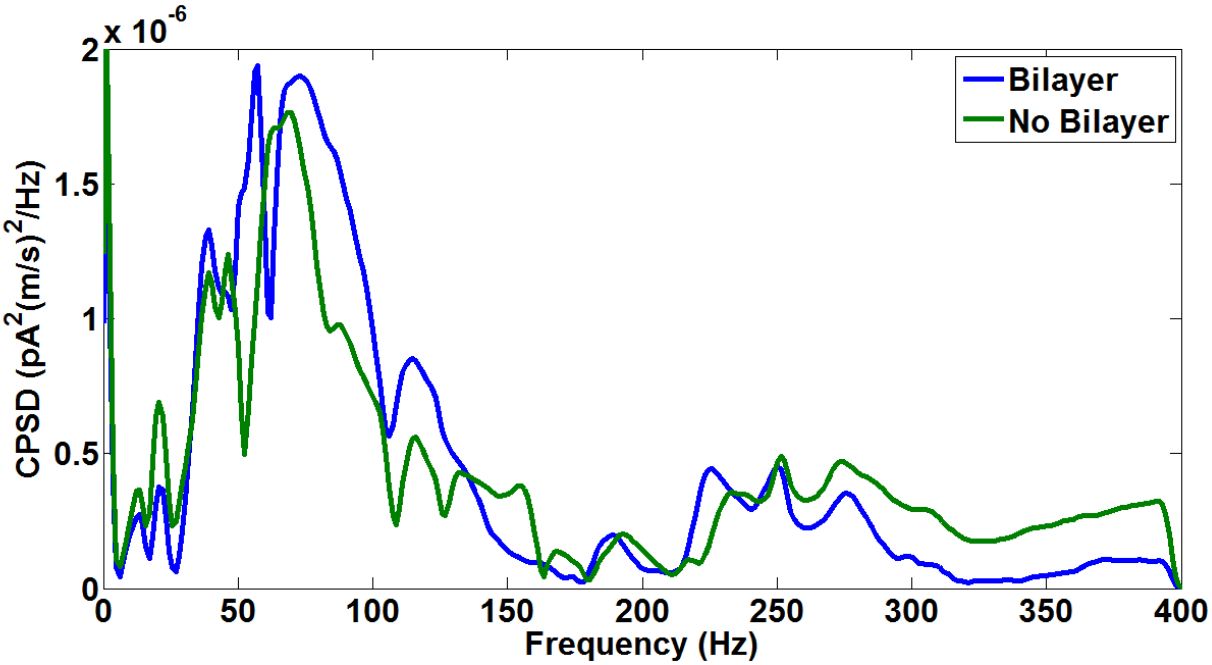

Figure 4-8. Cross-spectral power as a function of frequency of the AIHC and AIHC lacking a bilayer. The input to the ACE is a chirp signal with a linear frequency sweep from 1 to 400 Hz, repeated 4 times. The fluid velocity around the artificial stereocilium and the AIHC current act as the input and output components, respectively, of the cross power spectrum. The AIHC has 0 mV DC offset applied across its bilayers.

Figure 4-9 shows the coherence corresponding to the CPSD analysis in Figure 4-8. Similar to the results of the CPSD comparison, the AIHC and control case show little difference coherence across the frequency range. The coherence of each case is particularly important where the frequency response is highest, between 60 and 120 Hz. In this range, the AIHC has slightly

better coherence than the control case, but both show a low level of noise in the measurements. Therefore, it is likely that the fluid velocity around the stereocilium leads to the current generation in both of these cases. From the CPSD and coherence results, it can be concluded that the presence of a bilayer makes little difference in the current generation of the AIHC with 0 mV DC offset applied across its bilayer. This result is in line with the bilayer current generation theory discussed in Section 2.1. Referring to Equation (2-4), in the absence of an applied DC offset, the bilayer does not generate any current.

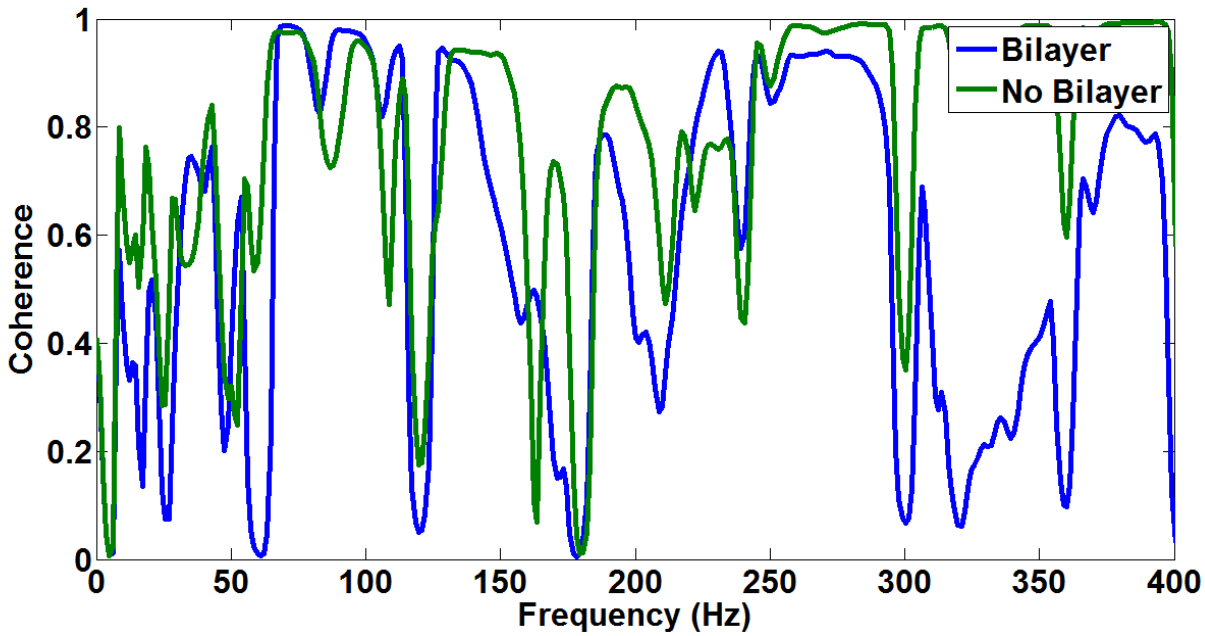

Figure 4-9. Coherence of the CPSD comparing the AIHC and AIHC lacking a bilayer. The corresponding CPSD is shown in Figure 4-8. Of particular importance is the coherence of each case where the frequency response is highest, between 60 and 120 Hz.

If the bilayer is not responsible for the current generation in the 0 mV DC offset case, the probe wires could be the source of the current. Physical movement of the probe wires of the AIHC electrical probe wires would generate current if the movement is large enough to be sensed by the Axopatch headstage. The construction of the AIHC and positioning of the hydrogels leaves a

small gap between the hydrogel and the substrate, as shown in Figure 3-1. This small portion of exposed probe wire could be shaking due to the movement of the artificial stereocilium and hydrogel. If the probe wires are shaking due to the sinusoidal flow, the current generated by the probe wires would be present in both the 0 mV DC offset case and the control case lacking a bilayer; such as in Figure 4-8. Therefore, it is concluded that for the AIHC created in this work, the current generated at 0 mV DC offset is not the result of the current generating properties of the bilayer. The results at 0 mV DC offset may not be consistent with the results at other DC offsets.

4.2.3 Effect of DC Offset

The CPSD analysis presented in Figure 4-10 compares the results of the AIHC with varying levels of DC offset. The general trend shows that the peak response increases as DC offset is increased. Besides the 0 mV DC offset case, the peak response frequency remains fairly constant at 83±1 Hz. The increase in peak response with DC offset supports the theory discussed in Section 2.1. As the DC offset increases, the presence of a single dominant peak becomes more prominent. This result can be attributed to the noise levels remaining constant between tests while the AIHC response at its dominant frequency increases with increasing DC offset. The maximum DC offset obtainable in these tests is 60 mV. For this particular AIHC bilayer, DC offset levels higher than 60 mV cause the bilayer to coalesce.

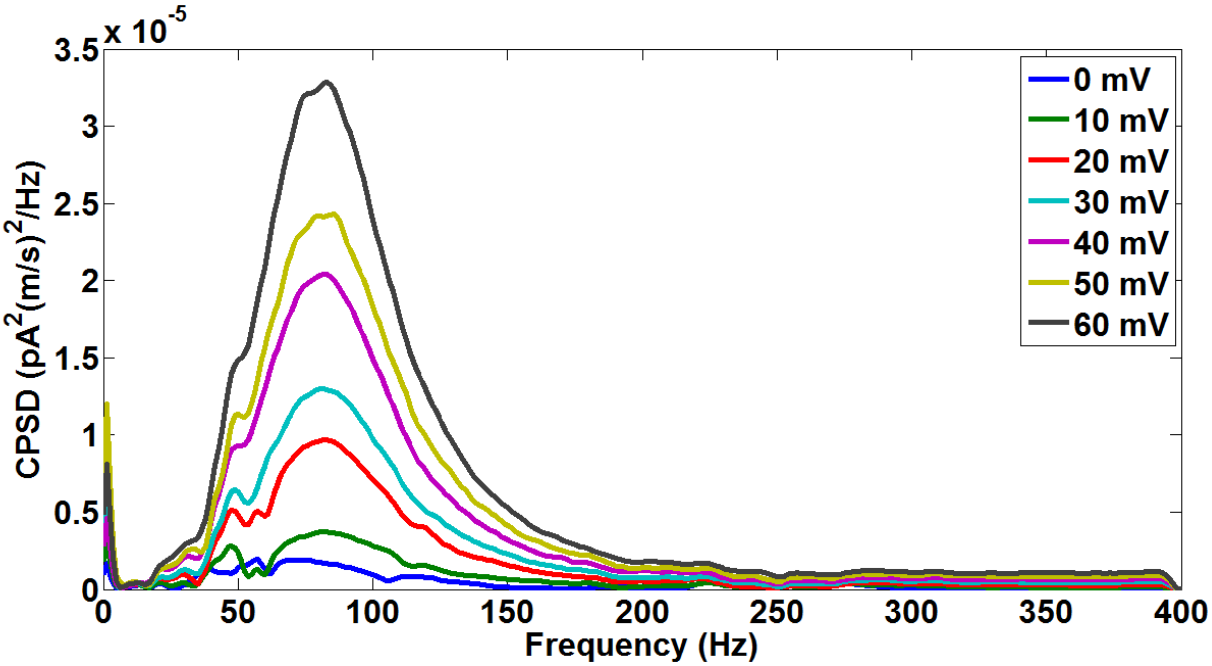

Figure 4-10. Cross-spectral power as a function of frequency of the AIHC with varying DC offset applied across the AIHC bilayer. The input to the ACE is a chirp signal with a linear frequency sweep from 1 to 400 Hz, repeated 4 times. The fluid velocity around the artificial stereocilium and the AIHC current act as the input and output components, respectively, of the cross power spectrum.

Figure 4-11 shows the coherence plot corresponding to the CPSD analysis in Figure 4-10. The coherence of the AIHC is critical where frequency response is highest, between 60 and 120 Hz. This frequency range can be seen more closely in Figure 4-12. For each of the DC offsets, the coherence is good around the frequency of optimal response. Increasing DC offset tends to show better coherence between input fluid velocity and output AIHC current, with the 50 mV DC offset being the only case to break the trend. This deviation from the trend can be attributed to the visibly noisier data collection that occurred during the 50 mV DC offset test, which may occur because of a poor test. The increase in coherence as DC offset increase is more pronounced at higher frequencies, where high DC offset cases (>10 mV) remain above 0.75 while the low DC offset cases (≤10 mV) fall below 0.75.

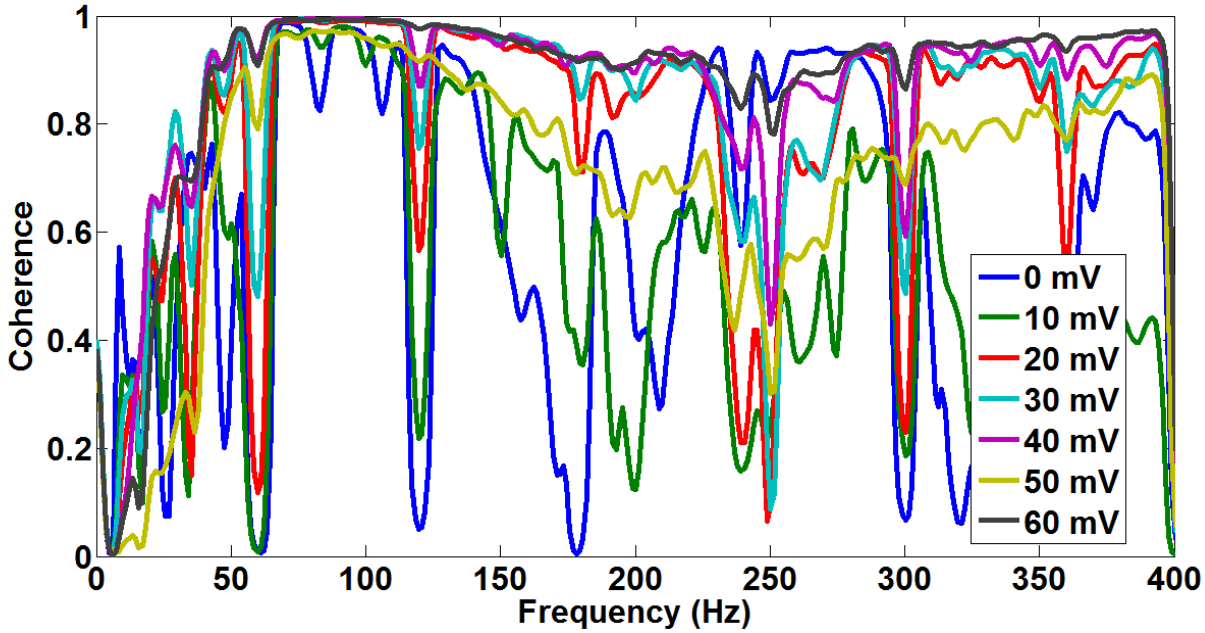

Figure 4-11. Coherence of the CPSD of the AIHC with varying DC offset. The corresponding CPSD is shown in Figure 4-10. Of particular importance is the coherence of each case where the frequency response is highest, between 60 and 120 Hz. A closer view of this important frequency range is shown in Figure 4-12.

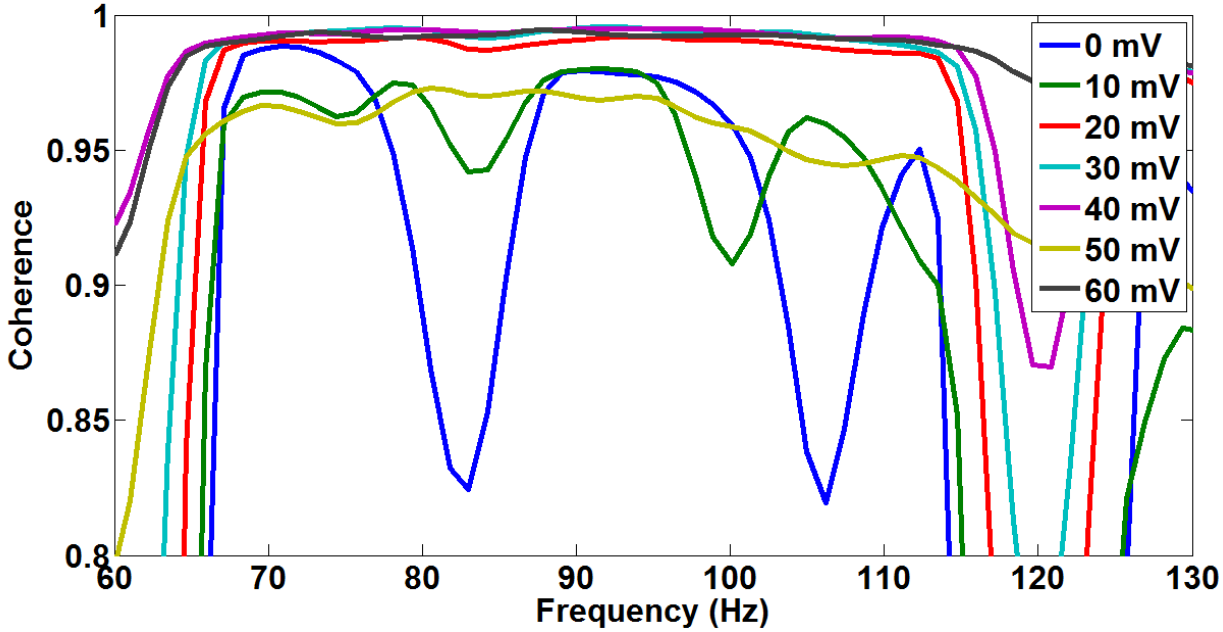

Figure 4-12. Coherence of the CPSD of the AIHC with varying DC offset. This image shows a closer view than Figure 4-11 of the frequency range where frequency response in the CPSD is highest.

Besides peak response, calculating broadband power is another useful analysis when evaluating the AIHC response. The broadband power, integrated from 25 to 400 Hz, from the CPSD in Figure 4-10 is displayed in Figure 4-13. As is the case with the CPSD peak, an increase in DC offset increases the broadband power. Two trend lines are also displayed in Figure 4-13. The cubic trend line is shown in red and has the coefficient corresponding to the squared term set to 0 to fit the relationship in Equation (2-4). The second trend line is shown in green and leaves out the data point at 0 mV DC offset. When the 0 mV DC offset case is left out, the linear trend line matches the rest of the data very well. The R^2 value for the cubic and linear trend lines are 0.9943 and 0.9908, respectively. Both R^2 values indicate excellent fits between the trend lines and the data. Referring back to Equation (2-4), the minimal difference between the linear and cubic R^2 values suggests that the voltage dependence of the lipid bilayer is of minor significance in the predication of the broadband power of the AIHC. Excluding the 0 mV DC offset case, which is shown in Section 4.2.2 to not produce current via the AIHC bilayer, allows the data to fit a linear trend. Therefore, it can be concluded that the AIHC broadband power increases linearly with DC offset.

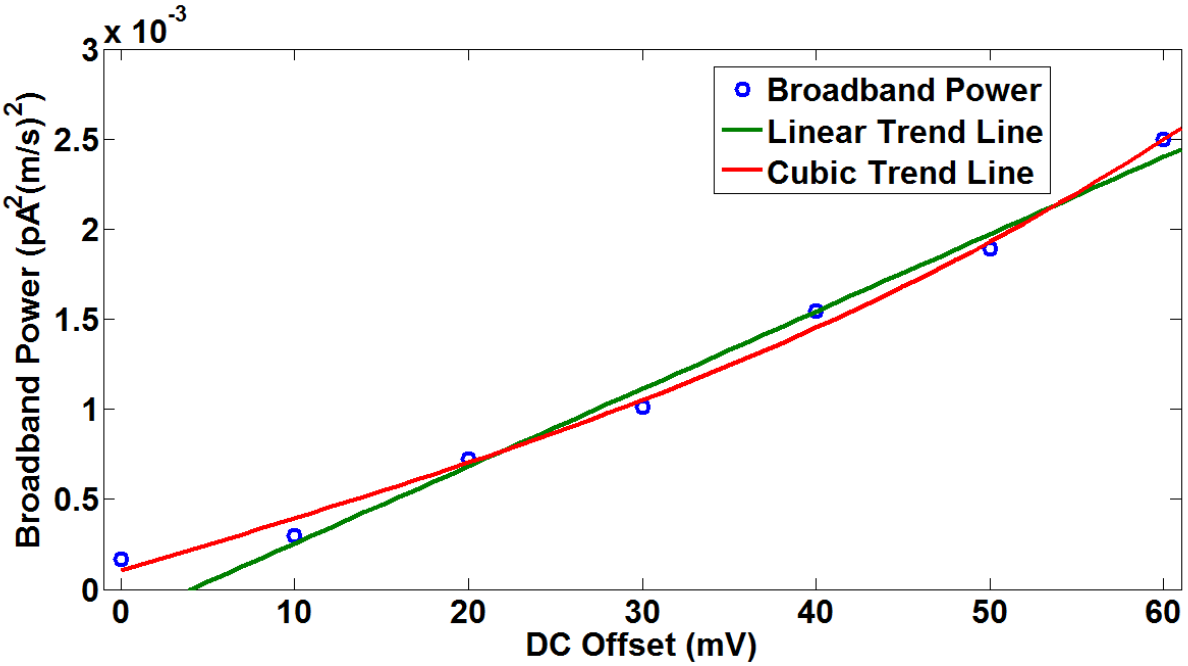

Figure 4-13. Broadband power of the CPSD of the AIHC with varying DC offset. Broadband power is calculated by integrating the CPSD from 25 to 400 Hz. The corresponding CPSD is shown in Figure 4-10. The cubic trend line has the coefficient corresponding to the squared term set to 0. The linear trend line leaves out the data point at 0 mV.

In addition to using a CPSD analysis, the response of the AIHC can be characterized by quantifying the current output as a function of fluid velocity input. The magnitude of the transfer function estimate, as calculated by MATLAB®, between the AIHC current output and fluid velocity input is displayed in Figure 4-14. A first peak for each DC offset case is seen at approximately 70 Hz. The transfer function estimate also appears to be approaching a second peak past 400 Hz, although input frequencies beyond 400 Hz are not tested in this work. Considering that coherence is high for frequencies approaching 400 Hz for most of the DC offset cases, as shown in Figure 4-11, the second peak is likely a direct response to the input fluid velocity and not a result of noise in the current measurements. The presence of more than one resonant frequency suggests that the AIHC behaves as a continuous system. As DC offset

increases, the overall transfer function estimate magnitude increases. This trend resembles that of the previous CPSD analysis.

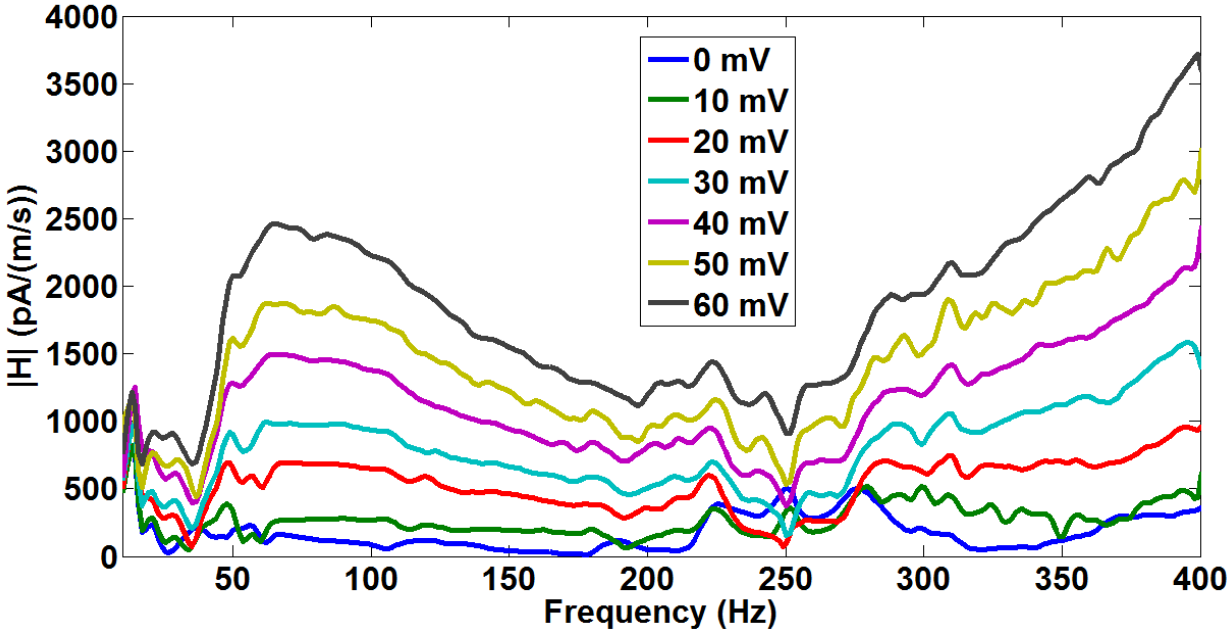

Figure 4-14. Magnitude of the transfer function estimate between the input fluid velocity and the AIHC output current with varying levels of applied DC offset. A peak at approximately 70 Hz is observed in each of the DC offset cases. The transfer function estimate appears to be approaching a second peak beyond 400 Hz.

4.2.4 Artificial Stereocilium Resonant Frequency

The resonant frequency of the AIHC artificial stereocilium can be determined by calculating the maximum cross-spectral power from the CPSD analysis. Observation of the CPSD analysis in Figure 4-10, however, shows that there is not a defined peak for every DC offset. Using cross-spectral power integration over a set frequency range with different center frequencies allows the determination of the frequency range with the highest power. For this analysis, the cross-spectral power is integrated over a range of 10 Hz, with center frequencies ranging from 70 to 90 Hz. The center frequency with the highest integrated power for each DC offset level is listed in Table 4-2. The highest power frequency of 73 Hz at 0 mV can be considered an outlier since its CPSD

peak in Figure 4-10 does not form a peak exhibiting the resonant behavior of the other DC offsets. The highest power frequency at 0 mV is also far away from the other peak frequencies. When only considering the DC offset levels from 10 to 60 mV, the average highest power frequency is approximately 83 Hz. Therefore, the resonant frequency of the AIHC artificial stereocilium is determined to be approximately 83 Hz.

Table 4-2. Center frequency with highest integrated spectral power for each DC offset. The cross-spectral power from the CPSD analysis is integrated over a 10 Hz range, centered at the center frequency. When determining the resonant frequency of the AIHC artificial stereocilium, the highest power center frequency at 0 mV DC offset can be considered an outlier.

DC Offset (mV)	**Center Frequency with Highest Power (Hz)**	**Integrated Power $* 10^4$ $(pA^2(m/s)^2)$**
0	73	0.20627
10	84	0.40280
20	83	1.0521
30	83	1.4132
40	82	2.2150
50	83	2.6513
60	82	3.5659

Calculation of the resonant frequency of the artificial stereocilium using the Rayleigh-Ritz method is detailed in Section 2.3. MATLAB® is used to perform the matrix calculations, solve the eigenvalue problem, and determine the natural frequency of the artificial stereocilium for the clamp-free and pinned-free cases. The MATLAB® code for each boundary condition is given in Appendix B.2. The predicted natural frequency using the Rayleigh-Ritz method and the clamped-free boundary condition assumption is 311.7 Hz. The predicted value is contained within the chirp signal used in the frequency tuning tests, and would be observed in the CPSD analysis if it were the true resonant frequency of the AIHC. However, the predicted value of 311.7 Hz is much higher than the tested value of approximately 83 Hz. The damping caused by

the hexadecane oil would reduce the natural frequency, but not by such a considerable amount. Such discrepancy between the predicted and tested resonant frequencies suggests that the clamped-free boundary condition assumption is invalid.

The second boundary condition under consideration is the pinned-free beam with a rotational spring attached to the pinned end. This boundary condition can be thought of as a non-ideal cantilever, where the rotational stiffness at the pinned end may be high but not perfectly cantilevered. Without a known value for the stiffness of the hydrogel, the rotational spring stiffness is varied in the eigenvalue problem outlined in Section 2.3 until the predicted and tested natural frequencies match. When equating the tested resonant frequency to the resonant frequency predicted by the pinned-free beam assumption, the rotational spring stiffness is $177 * 10^{-6}\ Nm/rad$. When compared to biological values, the rotational stiffness of the artificial stereocilium is approximately 12 orders of magnitude too large [39, 40]. However, matching the low rotational stiffness of the biological case is not a research objective of this work.

The main reason why the AIHC stereocilium departs from the ideal cantilever case is hypothesized to be hydrogel elasticity. The low predicted rotational stiffness is most likely a result of the hydrogel having a low Young's modulus. Jampole et al. created a finite element analysis (FEA) model of a hydrogel-based hair cell sensor similar to the AIHC [41]. They created FEA simulations for the range of hydrogel elasticity found in literature, from 1 to 90 kPa [42-44]. The group investigated how hair stiffness and hydrogel elasticity affected the synthetic hair's natural frequency. Their findings indicated that natural frequency decreased approximately 10-fold when decreasing the hydrogel elasticity from 90 to 1 kPa. They also mentioned that the resonant frequency of a hydrogel-based hair cell is difficult to predict because

of the difficulties in characterizing the hydrogel stiffness. For the work presented here, the low rotational stiffness of at the base of the artificial stereocilium can therefore likely be attributed to the hydrogel elasticity.

4.3 Variable Sensitivity Tests

Variable sensitivity tests are conducted to determine if the nonlinear gain in the human cochlea can be imitated by changing the DC offset applied across the AIHC's bilayer. A signal with variable voltage, from 1 to 10 V, and constant frequency, 105 Hz, is sent from the signal generator to shaker. 105 Hz is used as the input frequency because it falls within the frequency range where AIHC response is greatest, as shown in Figure 4-10. Figure 4-15 presents the results of the variable sensitivity tests. For each test, the DC offset is held constant while the fluid velocity around the stereocilium is increased in steps by increasing the voltage sent from the signal generator. For each new test, the DC offset is increased, up to the point that the bilayer coalesces. The bilayer in this case coalesces past 60 mV DC offset. A 4^{th} order band-pass filter with a center frequency of 105 Hz and a width of 2 Hz is applied to the time domain data to remove noise from the measurement. The RMS current, which is shown in Figure 4-15, is calculated from the filtered data.

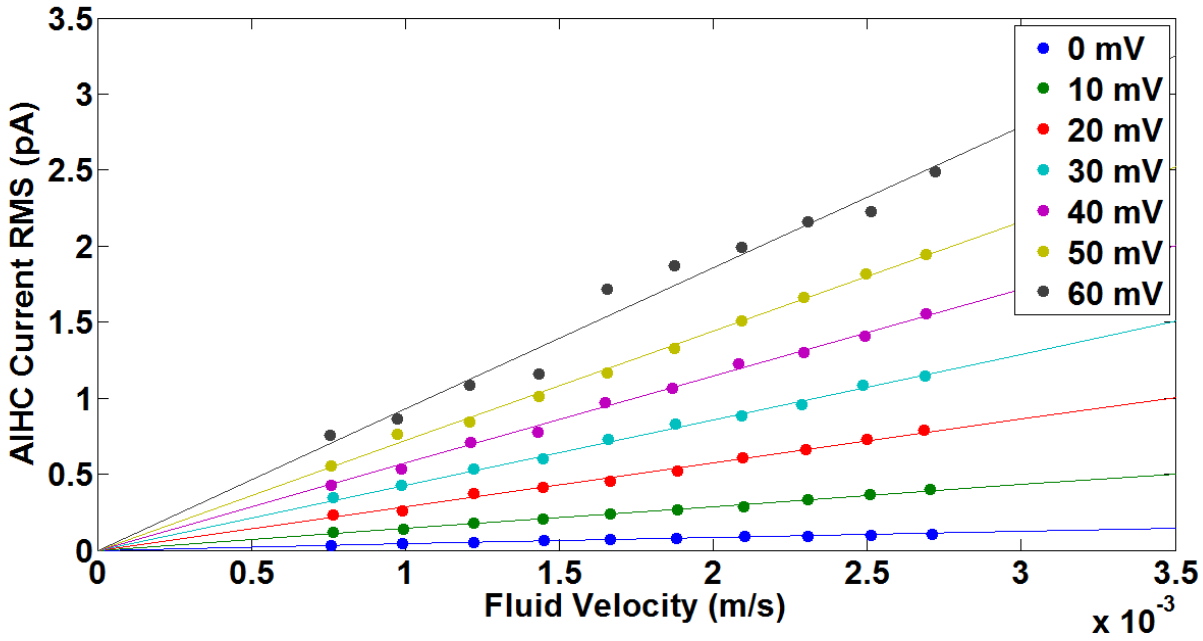

Figure 4-15. Response of the AIHC to changes in fluid velocity and DC offset at a constant input frequency of 105 Hz. The linear trend line going through the point (0, 0) for each DC offset is also shown in the figure. The data at 60 mV DC offset is noisy in the time domain and, as a result, does not fit the trend line as well as the lower DC offset cases.

The steps between the fluid velocities of each test remain fairly constant, which shows that the fluid velocity in the ACE can be easily controlled by changes in the signal generator voltage. The constant difference between fluid velocity steps also demonstrates the linearity between increases in shaker voltage and fluid velocity. This simple modulation of the fluid velocity allows for repeatable tests and comparable results between tests.

Also shown in Figure 4-15 are the linear trend lines for each DC offset. Following the assumption that the AIHC produces 0 current in the absence of fluid flow, the trend lines are forced to intersect with the plot origin. As can be expected from the results of Section 4.2.3, increases in DC offset result in an approximately linear increase in AIHC output. This linearity can be seen in the proximity of the data points to their respective linear trend lines. The 60 mV DC offset case, however, does not follow its trend line as closely. Visible inspection of the

AIHC time domain data at 60 mV shows that a large amount of noise is present in the signal, which results in a worse match between the RMS data points and trend line shown in Figure 4-15. The noisy data in the 60 mV DC offset test could have been caused by a poor test.

Well-defined relationships between the inputs and output of the AIHC, where fluid velocity and DC offset act as the inputs and AIHC current is the output, give the AIHC the unique characteristic of variable sensitivity. This variable sensitivity can be used to mimic the nonlinear gain found in the human cochlea, as discussed in Section 1.1. An example of a nonlinear gain curve resulting from manipulation of the DC offset is shown in Figure 4-16. At each fluid velocity in Figure 4-16, a DC offset is chosen to mimic the function of cochlear variable sensitivity. Similar to the shape of Figure 1-1, the AIHC current increases linearly at low fluid velocities, levels off at higher fluid velocities, and eventually decreases at the highest fluid velocity. The cubic polynomial trend line in Figure 4-16 is used simply to provide an easier view of the shape formed by the data points.

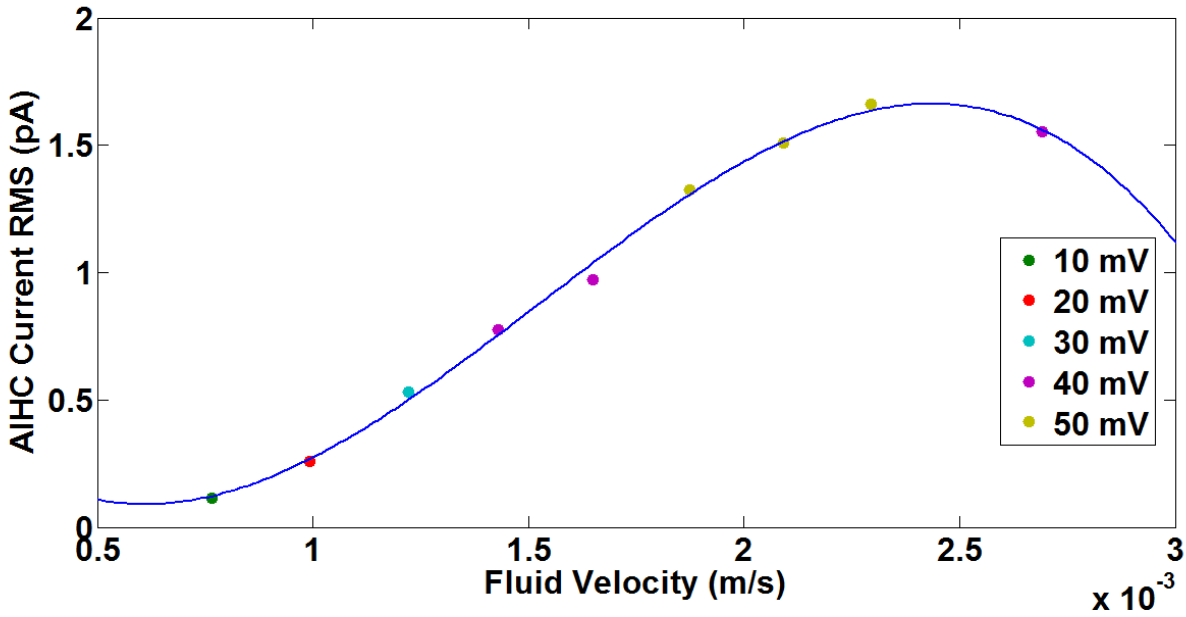

Figure 4-16. Select AIHC current responses from Figure 4-15. The DC offset at each fluid velocity is selected to imitate the variable sensitivity found in the human cochlea. The blue curve is a cubic trend line fit to the current data to fill in the gaps between fluid velocity steps. Similar to the shape of Figure 1-1, the AIHC current increases approximately linearly at low fluid velocities before levelling off and eventually decreasing at high fluid velocities.

5 Summary and Conclusions

5.1 Artificial Cochlear Environment

This work presented the results of creating and testing the ACE and AIHC. The primary goal of the ACE was to recreate the sinusoidal fluid flows found in the human cochlea. These fluid flows are characterized by a very low Reynolds number (5E-4), a low Womersley number (0.4), and a lack of nonlinearities and vortex shedding. As presented in Section 4.1, the ACE was able to create sinusoidal fluid flows with maximum Reynolds and Womersley numbers of 0.1797 and 2.379, respectively, at 79 Hz. Although these nondimensional parameters are not on the biological scale, they both are low enough to resemble the types of flows occurring in the human cochlea. Additionally, investigation into the maximum Keulegan-Carpenter number (<0.3) and frequency parameter (<5) showed that nonlinearities are not expected in the flow field. However, due to the characteristics of the modal shaker used in the test setup, the ACE should not be operated below 25 Hz as the sinusoidal fluid flows appear underdeveloped. The ACE is capable of providing controlled sinusoidal fluid flows from 25 to 400 Hz, with fluid velocities around the artificial stereocilium ranging from approximately 0.75 to 2.7 mm/s. The fluid velocity range in the ACE is shown in Figure 4-15.

Although the ACE was able to create the sinusoidal fluid flows necessary to test the resonant frequency of the AIHC, a few limitations persisted during testing. The first limitation of the test setup was the inability of the modal shaker to produce controlled sinusoidal fluid flows below 25 Hz. To test at lower frequencies, a different excitation method would need to be used, such as a piezoelectric actuator. The addition of higher frequency testing beyond 400 Hz would also allow for the investigation of the second peak in the transfer function estimate analysis. Another limitation of the current test setup is the lack of biological dynamic similitude caused by the

relatively high Reynolds and Womersley numbers. The Reynolds and Womersley numbers, both being an order of magnitude too large, would need to be lowered to reach the biological values in the human cochlea. Without changing the diameter of the AIHC artificial stereocilium, future test setups using the ACE would need to reduce the fluid velocity or increase the fluid's kinematic viscosity. Increasing the kinematic viscosity of the fluid in the ACE would also reduce the Womersley number to that of the biological case. If biological dynamic similitude were attained in future iterations of the ACE, the test setup could be deemed an accurate model of the fluid environment of the human cochlea.

5.2 Artificial Inner Hair Cell

Testing of the AIHC began with control tests used to determine which aspects of the AIHC were important to its current generation capabilities with 0 mV DC offset applied across the bilayer. During these frequency tuning tests, chirp signals with frequencies from 1 to 400 Hz were applied to the ACE. The first control test compared the AIHC to an AIHC lacking an artificial stereocilium. Both cases exhibited a peak in their CPSD plots at approximately 75 Hz, as shown in Figure 4-6. However, the spectral power of the AIHC was approximately 20 times greater than the control case lacking a stereocilium. When the AIHC was compared to a control case lacking a bilayer, both cases displayed similar results in their CPSD analyses. CPSD peaks at the same frequencies and of similar magnitudes are noted in Figure 4-8. Therefore, the current output from the AIHC at 0 mV DC offset does not result from bilayer mechanics. At 0 mV DC offset, the most critical component of the AIHC is the stereocilium, while the bilayer only plays a role in current generation at higher DC offsets.

When the DC offset across the lipid bilayer was increased in the remaining frequency tuning tests, the results showed that current output increased with bilayer potential, as presented in

Figure 4-10. Figure 4-13 shows that the relationship between broadband current output and DC offset increases linearly, thus showing that the bilayer's voltage dependence is minimal. The resonant frequency of the AIHC was approximately 83 Hz, with little variation between DC offset test cases. The resonant frequency of the 0 mV DC offset case was found to be 73 Hz and deemed an outlier. The transfer function estimate analysis indicated the presence of multiple peaks in the transfer function between input fluid velocity and AIHC current output, with one of the peaks beyond 400 Hz. The final objective of this research was to determine if the AIHC could mimic the variable sensitivity found in the human cochlea. The general shape of the human cochlea's nonlinear response was recreated with the AIHC in Figure 4-16, which has a linear response at low fluid velocities and a decreasing response at high fluid velocities.

Overall the AIHC met its goals of detecting sinusoidal fluid flows, detecting different fluid velocities and frequencies, responding to increased DC offset, and imitating the nonlinear gain characteristics found in the human cochlea. The AIHC detailed in this work is a step forward for creating bio-inspired hair cell sensors which can operate in a realistic cochlear environment. However, the design of the AIHC could be improved to better replicate biological inner hair cells. The first consideration in redesigning the AIHC is to decrease the diameter and length of the artificial stereocilium. Reducing the artificial stereocilia diameter would help decrease the Reynolds number to the biological scale.

Another improvement of the AIHC would be to increase the rotational stiffness between the artificial stereocilium and the base of the AIHC substrate. Future designs of the AIHC will likely incorporate multiple artificial stereocilium of different thicknesses and lengths to respond to multiple resonant frequencies. In the current design of the AIHC, the rotational stiffness is $177 * 10^{-6}\ Nm/rad$. This stiffness is so low that increasing the thickness, and subsequently

stiffness, of the artificial stereocilium actually decreases its resonant frequency. This result demonstrates how the rotational stiffness is so low that the artificial stereocilium mass plays a larger role than artificial stereocilium stiffness in determining the resonant frequency. Increasing the rotational stiffness would let the stereocilium be the dominant stiffness in the system and allow the artificial stereocilium to be more easily tuned to particular resonant frequencies of interest. As noted by Jampole et al., when hydrogel stiffness is low enough, the artificial stereocilium stiffness plays almost no role in the resonant frequency [41]. Therefore, the hydrogel stiffness of the current AIHC needs to be increased or the AIHC fabrication needs to be modified to add other forms of structural stiffness to the artificial stereocilium.

Appendix A: Artificial Inner Hair Cell and Artificial Cochlear Environment Dimensions and Parameters

The initial dimensions of the polyurethane substrate were varied until the RAM screws could reliably separate and join together the lipid droplets without deforming the soft hydrogels. The final set of substrate dimensions is given in Figure A-1.

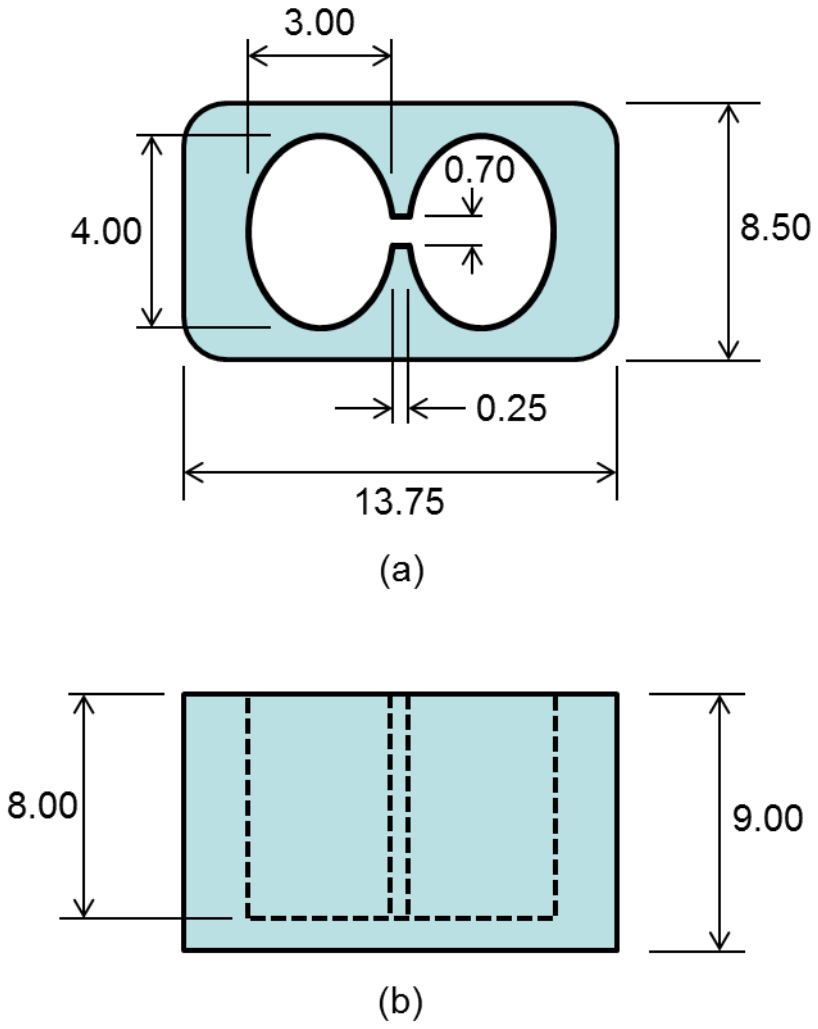

Figure A-1. Diagram of the artificial inner hair cell substrate dimensions. (a) shows the top view of the substrate. (b) shows the front view of the substrate. All dimensions are in mm. Figure is not drawn to scale.

A glass pipette puller is used to form the hairs and cause the tapered shape. The glass hair and hydrogel dimensions are listed in Figure A-2. A handheld UV light cures the hydrogel solution to form the hydrogels. When forming the hydrogel that acts as the root of the artificial hair, the hair is held in a vertical orientation during the curing process. The UV light positioning and steps used to cure the hydrogel are given in Table A-1.

.

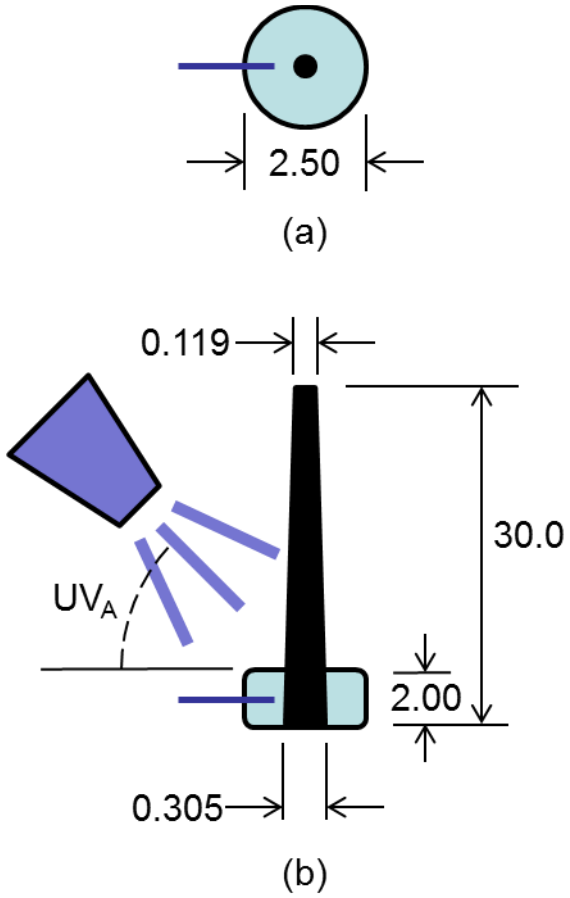

Figure A-2. Diagram of the hydrogel and artificial stereocilium used in the artificial hair cell sensor. (a) displays the top view of the hydrogel while (b) displays the front view and the orientation of the UV light. UV_A is the angle of the UV light from horizontal. All dimensions are in mm. Figure is not drawn to scale.

Table A-1. Hydrogel curing process steps.

Hydrogel Type	**Step**	**UV Light Angle - UV_A (°)**	**Time (min)**
With Stereocilium	1	45	1
	2	135	1
	3	45	3
	4	135	3
Without Stereocilium	1	90	3

The dimensions of the ACE are given in Figure A-3. A cutout for the hair cell substrate is located at the bottom of the channel while inlet and outlet fluid fill ports are located at the top and side of the channel. Three square flanges are attached to the substrate cutout and each end of the channel. The RAM substrate holder attaches to the bottom flange to hold the AIHC's artificial stereocilium in the middle of the fluid channel.

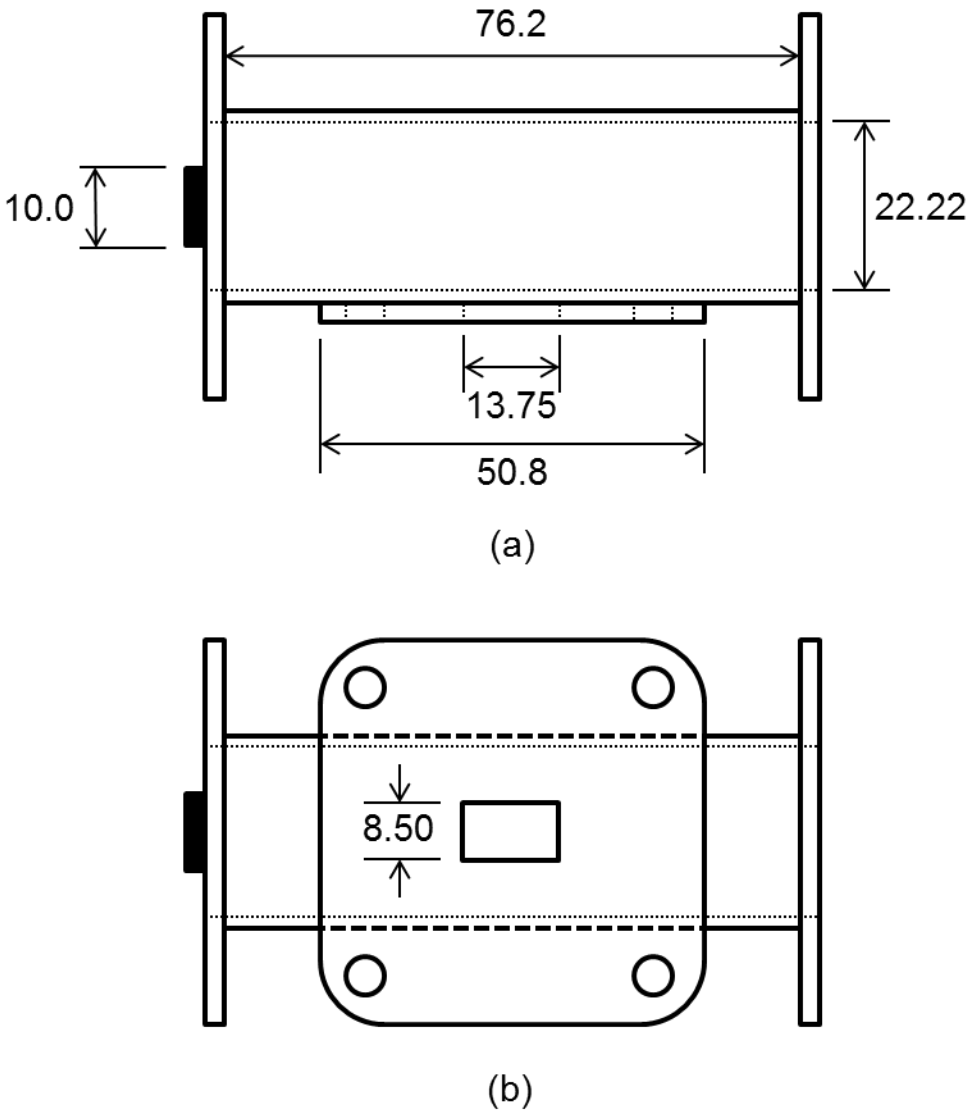

Figure A-3. Diagram of the artificial cochlear environment. (a) shows the front view of the ACE while (b) shows the bottom view. The diameter of the circular plug is given in (a) on the left. The square flange width is 50.8 mm and is equal for the three flanges, one on the left and right sides and one on the bottom.

Appendix B: MATLAB® Code

B.1 Velocity Profile in the ACE

```
%% Velocity profile around artificial stereocilium
% from paper: "Unsteady, laminar, incompressible flow through rectangular
% ducts" by Chien Fan
clc
close all

a = 0.0111125; % half of duct width (m)
b = a;         % half of duct height (m) - equal to duct half of duct width
nu = 3.935e-6; % fluid kinematic viscosity (m^2/s)
rho = 770;     % fluid density (kg/m^3)

f = 25; % pressure gradient frequency (Hz)
T = 1/f; % pressure gradient period (s)
om = 2*pi*f; % pressure gradient frequency (rad/s)
p = a*b*om/nu; % psi from paper

w1 = 0;
maxw = 0;

kstep = 0.05; % size of ksi steps (ksi from paper)
              % 0.05 = 20 steps along half width of duct (40 total steps)
zstep = 0.05; % size of zeta steps (zeta from paper)
              % 0.05 = 20 steps along half height of duct (40 total steps)
tstep = T/4; % Velocity profile snapshot taken at 1/4 of period (maximum)
what = zeros(1/zstep+1);

figure('Renderer','zbuffer');
set(gca,'NextPlot','replaceChildren');
caxis([-1.5 1.5])

t = tstep;
for ki = 0:1/kstep
    k = ki*kstep;
    for zi = 0:1/zstep
        z = zi*zstep;
        for m = 0:100 % for integration from 0 to 100
            for n = 0:100
                % paper eq 17a
                m_n = ( p*pi^2/4 * ((2*m+1)^2 + (2*n+1)^2) * cos(om*t) +
p^2*sin(om*t) ) / ( p^2 + pi^4/16 * ((2*m+1)^2 + (2*n+1)^2)^2 );
                % paper eq 17
                w1 = w1 + (-1)^(m+n) / ( (2*m+1)*(2*n+1) )...
                     * cos( (2*m+1) * pi * k / 2 )...
                     * cos( (2*n+1) * pi * z / 2 )...
                     * m_n;
            end
        end
        what(ki+1,zi+1) = w1 * 16/pi^2; % nondimensional fluid velocity
        w1 = 0;
```

```
    end
end

% fluid velocity is symetric about center (4 quadrants are equal)
whatp = what(2:length(what), 2:length(what));
what1 = flipud(whatp);
what2 = fliplr(what1);
what4 = what;
fill = flipud(what4(2:length(what4),1));
what3 = [fill';
         fliplr(whatp);];

whatcomb = [what2 fill what1;
            what3      what4];

k = -1:kstep:1;
z = -1:zstep:1;

% Plot velocity profile
figure(1)
surf(k,z,whatcomb)
xlabel('Horizontal Position')
ylabel('Vertical Position')
zlabel('Nondimensional Fluid Velocity')
title('f = 25 Hz')
zlim([0 1.5])
set(gca,'nextplot','replacechildren');

set(findall(gcf,'type','text'),'fontSize',20)
set(findall(gcf,'type','axes'),'fontSize',20,'LineWidth',3)
```

B.2 Rayleigh Ritz Method for Predicting Artificial Stereocilium Resonant Frequency

```
%% Rayleigh Ritz method for cylindrical tapered beam with cantilever or
%  rotational spring at the base, and free at the tip
%
% Inputs: base diameter (mm), tip diameter (mm), length (mm),
%         torsional spring constant (N*m/rad)
%         - if the torsional spring constant is 0, a cantilever beam is
%           assumed.  for all other values, a rotational spring is assumed
%           at the base of the beam
%
% Output: Matrix of natural frequencies

function [fsols] = RR_TaperBeam(db, dt, l, tau)
syms x
p = 2230; % Density (kg/m^3)
p = p + 770; % Density including effects of surrounding hexadecane oil
EE = 62.8e9; % Elastic modulus (Pa)
```

```
db = db*.001; % Convert to meters
dt = dt*.001;
l = l*.001;
c = (db-dt)/l; % Slope of taper
mx= p*(pi/4)*(db-c*x)^2; % Mass per unit length (kg/m)
eix = EE*(pi/64)*(db-c*x)^4; % Rigidity per unit length

% Set of admissible funtions
if tau == 0 % Cantilever beam
    phi = [x^2, x^3, x^4, x^5, x^6, x^7, x^8, x^9];
else % Rotational spring at base
    phi = [(x/l)^1, (x/l)^2, (x/l)^3, (x/l)^4, (x/l)^5, (x/l)^6, (x/l)^7,
(x/l)^8];
end

N = length(phi);

% Generate stiffness and mass matrices using Rayleigh-Ritz method
kks = zeros(N,N);
mms = zeros(N,N);
dphi = diff(phi,x,1);
ddphi = diff(dphi,x,1);
for i=1:N
    for j=1:N
        if (j < i)
            kks(i,j)=kks(j,i);
            mms(i,j)=mms(j,i);
        else
            Vmaxs=int(eix*ddphi(i)*ddphi(j),0,l)+tau*dphi(i)*dphi(j);
            kks(i,j)= subs(Vmaxs,x,0);
            Trefs=int(mx*phi(i)*phi(j),0,l);
            mms(i,j)=eval(Trefs);
        end
    end
end
format('shortG');

% Solve eigenvalue problem
Fsols = sqrt(eig(kks,mms))/(2*pi);
```

References

[1] Hall, J. E., 2010, Guyton and Hall Textbook of Medical Physiology: Enhanced E-book, Saunders.

[2] Guinan Jr, J. J., 2012, "How are inner hair cells stimulated? Evidence for multiple mechanical drives," *Hearing Research*.

[3] Dallos, P., 1985, "Response characteristics of mammalian cochlear hair cells," *The Journal of neuroscience*, **5**(6), pp. 1591-1608.

[4] Chadwick, R. S., 1975, "Experimental observations of a mechanical cochlear model," *The Journal of the Acoustical Society of America*, **58**(3), p. 706.

[5] Cancelli, C., 1985, "Experimental results in a physical model of the cochlea," *Journal of fluid mechanics*, **153**, p. 361.

[6] Lechner, T. P., 1993, "A hydromechanical model of the cochlea with nonlinear feedback using PVF2 bending transducers," *Hearing Research*, **66**(2), pp. 202-212.

[7] Zhou, G., 1993, "A life-sized physical model of the human cochlea with optical holographic readout," *The Journal of the Acoustical Society of America*, **93**(3), p. 1516.

[8] Hemmert, W., Dürig, U., Despont, M., Drechsler, U., Genolet, G., Vettiger, P., and Freeman, D., "A life-sized hydrodynamical, micromechanical inner ear," Proc. Biophysics of the Cochlea. From Molecules to Models, pp. 409-416.

[9] Lim, K.-M., 2000, "Physical and mathematical cochlear models," Ph.D. 9986475, Stanford University, United States -- California.

[10] White, R. D., 2005, "Microengineered hydromechanical cochlear model," *Proceedings of the National Academy of Sciences - PNAS*, **102**(5), pp. 1296-1301.

[11] Wittbrodt, M. J., 2006, "Developing a physical model of the human cochlea using micro-fabrication methods," *Audiology & neurotology*, **11**(2), pp. 104-112.

[12] Chen, F., 2006, "A hydromechanical biomimetic cochlea: Experiments and models," *The Journal of the Acoustical Society of America*, **119**(1), p. 394.

[13] Liu, S., Gauthier, D. A., Mandelup, E., and White, R. D., 2008, "Experimental Investigation of a Hydromechanical Scale Model of the Gerbil Cochlea," *ASME Conference Proceedings*, **2008**(48722), pp. 277-284.

[14] Dunlap, M., 2013, "Experimental Measurement of the Utricle's Dynamic Response and the Mechanoelectrical Characterization of a Micron-Sized Droplet Interface Bilayer," Doctor of Philosophy, Virginia Polytechnic Institute and State University.

[15] Garrison, K. L., Sarles, S. A., and Leo, D. J., "Formation, encapsulation, and validation of membrane-based artificial hair cell sensors," Proc. SPIE Smart Structures and Materials+

Nondestructive Evaluation and Health Monitoring, International Society for Optics and Photonics, pp. 83390B-83390B-83313.

[16] Pinto, P. A., 2012, "Novel Bio-inspired Aquatic Flow Sensors," DTIC Document.

[17] Sarles, S. A., and Leo, D. J., 2010, "Regulated attachment method for reconstituting lipid bilayers of prescribed size within flexible substrates," *Analytical chemistry*, **82**(3), pp. 959-966.

[18] Sarles, S. A., and Leo, D. J., 2010, "Physical encapsulation of droplet interface bilayers for durable, portable biomolecular networks," *Lab on a Chip*, **10**(6), pp. 710-717.

[19] Sarles, S. A., Madden, J. D., and Leo, D. J., 2011, "Hair cell inspired mechanotransduction with a gel-supported, artificial lipid membrane," *Soft matter*, **7**(10), pp. 4644-4653.

[20] Young, T. T., 2012, "Lipid Bilayer Formation in Aqueous Solutions of Ionic Liquids," Virginia Polytechnic Institute and State University.

[21] Creasy, M., and Leo, D., 2010, "Non-invasive measurement techniques for measuring properties of droplet interface bilayers," *Smart materials and structures*, **19**(9), p. 094016.

[22] Hwang, W. L., Holden, M. A., White, S., and Bayley, H., 2007, "Electrical behavior of droplet interface bilayer networks: experimental analysis and modeling," *Journal of the American Chemical Society*, **129**(38), pp. 11854-11864.

[23] Requena, J., and Haydon, D., 1975, "The Lippmann equation and the characterization of black lipid films," *Journal of Colloid and Interface Science*, **51**(2), pp. 315-327.

[24] White, S., and Chang, W., 1981, "Voltage dependence of the capacitance and area of black lipid membranes," *Biophysical journal*, **36**(2), p. 449.

[25] Munson, B. R., Young, D. F., and Okiishi, T. H., 2006, Fundamentals of fluid mechanics, New York.

[26] Womersley, J. R., 1955, "Method for the calculation of velocity, rate of flow and viscous drag in arteries when the pressure gradient is known," *The Journal of physiology*, **127**(3), pp. 553-563.

[27] Iliadis, G., and Anagnostopoulos, P., 1998, "Viscous oscillatory flow around a circular cylinder at low Keulegan–Carpenter numbers and frequency parameters," *International journal for numerical methods in fluids*, **26**(4), pp. 403-442.

[28] Fan, C., and Chao, B.-T., 1965, "Unsteady, laminar, incompressible flow through rectangular ducts," *Zeitschrift für angewandte Mathematik und Physik ZAMP*, **16**(3), pp. 351-360.

[29] Yamanaka, G., Kikura, H., Takeda, Y., and Aritomi, M., 2002, "Flow measurement on an oscillating pipe flow near the entrance using the UVP method," *Experiments in fluids*, **32**(2), pp. 212-220.

[30] Gerrard, J., and Hughes, M., 1971, "The flow due to an oscillating piston in a cylindrical tube: a comparison between experiment and a simple entrance flow theory," *J. Fluid Mech*, **50**(1), pp. 97-106.

[31] Meirovitch, L., 1980, Computational methods in structural dynamics, Springer.

[32] Blevins, R. D., 1979, "Formulas for natural frequency and mode shape."

[33] Bayley, H., Cronin, B., Heron, A., Holden, M. A., Hwang, W. L., Syeda, R., Thompson, J., and Wallace, M., 2008, "Droplet interface bilayers," *Molecular BioSystems*, **4**(12), pp. 1191-1208.

[34] Baumgart, J., Fleischer, M., Yarin, Y., Grundmann, R., and Carus, U. C. G., 2007, "Fluid flow around stereocilia," *8th ISAIF, Lyon*.

[35] Jenkins, S., 2012, "CRC Handbook of Chemistry and Physics, 93rd ed," *Chemical engineering (New York)*, **119**(9), p. 9.

[36] Schmid, H., 2012, "How to use the FFT and Matlab's pwelch function for signal and noise simulations and measurements."

[37] Inman, D. J., 2010, "Engineering vibrations."

[38] Brüel&Kjær, "Type 4810 Mini-Shaker."

[39] Howard, J., and Ashmore, J. F., 1986, "Stiffness of sensory hair bundles in the sacculus of the frog," *Hearing Research*, **23**(1), pp. 93-104.

[40] Spoon, C., and Grant, W., 2011, "Biomechanics of hair cell kinocilia: experimental measurement of kinocilium shaft stiffness and base rotational stiffness with Euler–Bernoulli and Timoshenko beam analysis," *The Journal of experimental biology*, **214**(5), pp. 862-870.

[41] Jampole, E., Spurgeon, N., Avant, T., and Farinholt, K., 2012, "Characterization of Bio-Inspired Synthetic Hair Cell Sensors," Topics in Modal Analysis II, Volume 6, Springer, pp. 137-152.

[42] Chen, Q., Suki, B., and An, N., "Dynamic mechanical properties of agarose gel by a fractional derivative model," Proc. Proc. Summer Bioengineering Conf., Sonesta Beach Resort, Key Biscayne, Florida, USA, pp. 25-29.

[43] Chippada, U., 2010, "Non-intrusive characterization of properties of hydrogels," Rutgers, The State University of New Jersey.

[44] Yamaoka, H., Asato, H., Ogasawara, T., Nishizawa, S., Takahashi, T., Nakatsuka, T., Koshima, I., Nakamura, K., Kawaguchi, H., and Chung, U. i., 2006, "Cartilage tissue engineering using human auricular chondrocytes embedded in different hydrogel materials," *Journal of Biomedical Materials Research Part A*, **78**(1), pp. 1-11.